

Temperature structures in Galactic center clouds

Direct evidence for gas heating via turbulence[★]

K. Immer¹, J. Kauffmann², T. Pillai², A. Ginsburg¹, and K. M. Menten²

¹ European Southern Observatory, Karl-Schwarzschild-Strasse 2, 85748 Garching bei München, Germany
e-mail: ksimmer09@gmail.com

² Max-Planck-Institut für Radioastronomie, Auf dem Hügel 69, 53121 Bonn, Germany

Received 22 April 2016 / Accepted 5 July 2016

ABSTRACT

The central molecular zone at the center of our Galaxy is the best template to study star formation processes under extreme conditions, similar to those in high-redshift galaxies. We observed on-the-fly maps of para-H₂CO transitions at 218 GHz and 291 GHz towards seven Galactic center clouds. From the temperature-sensitive integrated intensity line ratios of H₂CO(3_{2,1}–2_{2,0})/H₂CO(3_{0,3}–2_{0,2}) and H₂CO(4_{2,2}–3_{2,1})/H₂CO(4_{0,4}–3_{0,3}) in combination with radiative transfer models, we produce gas temperature maps of our targets. These transitions are sensitive to gas with densities of $\sim 10^5$ cm⁻³ and temperatures <150 K. The measured gas temperatures in our sources are all higher (>40 K) than their dust temperatures (~ 25 K). Our targets have a complex velocity structure that requires a careful disentanglement of the different components. We produce temperature maps for each of the velocity components and show that the temperatures of the components differ, revealing temperature gradients in the clouds. Combining the temperature measurements with the integrated intensity line ratio of H₂CO(4_{0,4}–3_{0,3})/H₂CO(3_{0,3}–2_{0,2}), we constrain the density of this warm gas to 10^4 – 10^6 cm⁻³. We find a positive correlation between the line width of the main H₂CO lines and the temperature of the gas, direct evidence for gas heating via turbulence. Our data is consistent with a turbulence heating model with a density of $n = 10^5$ cm⁻³.

Key words. Galaxy: center – ISM: molecules – ISM: structure – ISM: clouds – submillimeter: ISM

1. Introduction

The central region of the Milky Way, the so-called central molecular zone (CMZ), is an exceptional star-forming environment. This region contains $\sim 10\%$ of the Galaxy's total molecular gas and produces 5–10% of the Galaxy's infrared and Lyman continuum luminosity (Morris & Serabyn 1996). The conditions (pressure, magnetic field strength, turbulence, gas temperature, etc.) in this region are much more extreme than in Galactic plane clouds (Morris & Serabyn 1996). The star formation rate in the CMZ is a factor of 10–100 lower than expected for the huge amount of dense gas and dust contained in this region (e.g. Yusef-Zadeh et al. 2009; Immer et al. 2012; Longmore et al. 2013; Kruijssen & Longmore 2013).

The high gas temperatures are one of the key properties of the CMZ clouds, influencing the chemistry of the gas, as well as the star formation efficiency of the clouds. It determines the thermal Jeans mass as well as the sound speed that in turn sets the Mach number. Understanding the gas temperature structure of Galactic center clouds is thus crucial for understanding the fragmentation and star forming mechanisms within them. The discrepancy between observed dust and gas temperatures is a long-known feature of CMZ clouds. While multi-wavelength observations of the dust emission in the CMZ yield dust

temperatures of ~ 20 K (Lis et al. 1999; Molinari et al. 2011), comparable to the dust temperatures of Galactic plane clouds, the gas temperatures are much higher (>50 K, Güsten et al. 1981; Hüttemeister et al. 1993; Ao et al. 2013; Mills & Morris 2013; Ott et al. 2014; Ginsburg et al. 2016). Many previous gas temperature measurements in the CMZ are based on observations of the NH₃ molecule which traces low-density gas ($n \sim 10^3$ cm⁻³, e.g. Güsten et al. 1981; Hüttemeister et al. 1993; Ott et al. 2014). Ao et al. (2013) mapped the inner ~ 75 pc of the CMZ in the para-H₂CO transitions at 218 GHz, sensitive to warmer ($T > 20$ K) and denser ($n \sim 10^4$ – 10^5 cm⁻³) gas. Their results show high gas temperatures towards many CMZ clouds, comparable to those measured in prior studies. This survey was extended to the whole CMZ ($-0.4^\circ < l < 1.6^\circ$) by Ginsburg et al. (2016). The inferred gas temperatures range from ~ 60 K to >100 K, where the highest values are measured towards Sgr B2, the 20 and 50 km s⁻¹ clouds, and G0.253+0.016 (The Brick). Comparing their results with dust temperature measurements of the whole CMZ, they show that the gas is uniformly hotter than the dust. The high gas temperatures are consistent with heating through turbulence, while uniform cosmic ray heating is excluded as a dominant heating mechanism.

H₂CO is a slightly asymmetric rotor molecule. It has two different species (i.e. ortho and para) for which the K_a^1 quantum number is odd or even. These two species are not connected by radiative transitions. The differences in the population of levels separated by $\Delta K_a = 2 \cdot n$ are due to collisions.

¹ K_a is the projection of J along the symmetry axis for the limiting case of a prolate (oblate) top.

[★] Integrated intensity maps of the H₂CO lines (Figs. E.1–E.7), ratio and uncertainty maps (Figs. F.1–F.7), and temperature and uncertainty maps (Figs. H.1–H.7) are only available at the CDS via anonymous ftp to cdsarc.u-strasbg.fr (130.79.128.5) or via <http://cdsarc.u-strasbg.fr/viz-bin/qcat?J/A+A/595/A94>

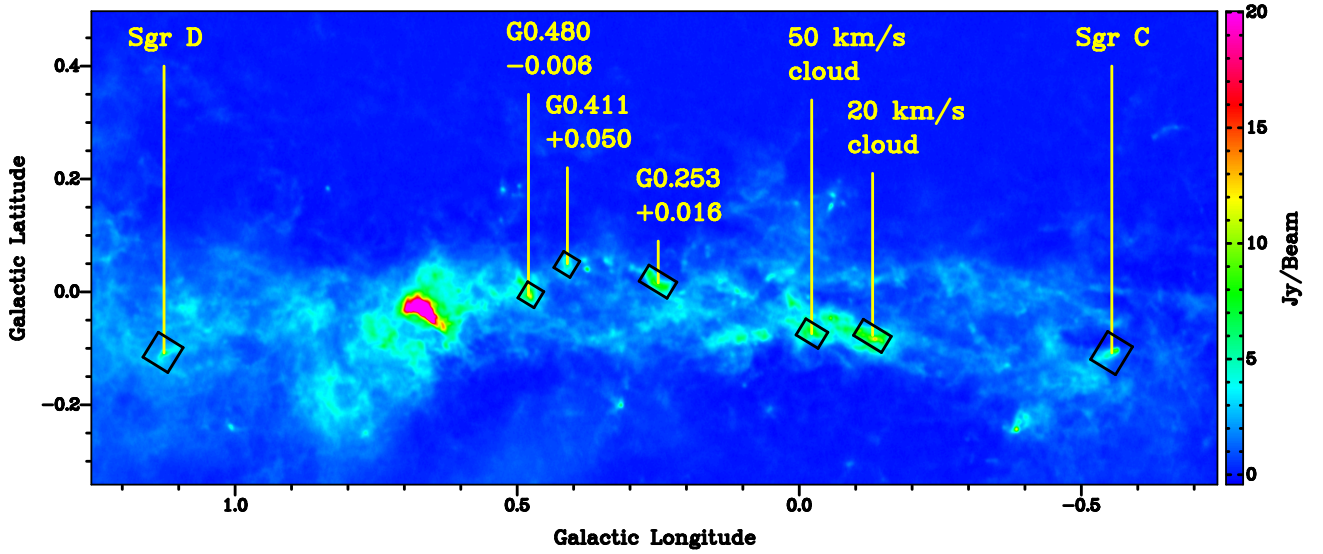


Fig. 1. 870 μm emission of the CMZ from the ATLASGAL survey (Schuller et al. 2009). The targets of our temperature study are marked. The boxes show the sizes of the observed OTF maps at 218 GHz for the 20 and 50 km s^{-1} clouds, G0.253+0.016, G0.411+0.050, and G0.480–0.006, and at 291 GHz for Sgr C and Sgr D.

Table 2. Properties of covered para- H_2CO transitions.

Transition	ν (GHz)	E_{up} (K)
$3_{0,3}-2_{0,2}$	218.22219	20.96
$3_{2,2}-2_{2,1}$	218.47563	68.09
$3_{2,1}-2_{2,0}$	218.76007	68.11
$4_{0,4}-3_{0,3}$	290.62341	34.90
$4_{2,3}-3_{2,2}$	291.23778	82.07
$4_{2,2}-3_{2,1}$	291.94806	82.12

Notes. Columns give quantum numbers, J_{K_a, K_c} , frequencies and level energies above the ground state. The critical densities of $3_{0,3}-2_{0,2}$ and $4_{0,4}-3_{0,3}$ are $\sim 6 \times 10^5 \text{ cm}^{-3}$ and $\sim 1 \times 10^6 \text{ cm}^{-3}$, respectively (Shirley 2015).

2.2. Baseline subtraction

The 218 GHz spectra were strongly affected by bad baselines (Fig. A.1). Since the baselines could not be cleanly removed by fitting low-level polynomials to the data, we fitted the spectra with splines over the velocity ranges -90 – 250 km s^{-1} for the 20 km s^{-1} cloud, G0.253+0.016, G0.411+0.050, and G0.480–0.006, and -60 – 220 km s^{-1} for the 50 km s^{-1} cloud. First, the raw data were smoothed to a velocity resolution of $\sim 0.9 \text{ km s}^{-1}$, then lines in the spectra were fitted with Gaussians and removed from the spectra if they were at least a 3σ detection. Then, the data were downsampled to a resolution of $\sim 36 \text{ km s}^{-1}$ to ensure that weak line emission that was not removed in the previous step would be smoothed out over the adjacent channels. This spectrum was then resampled to the original resolution of 0.9 km s^{-1} , yielding the spline spectrum, and then subtracted from the input spectrum. However, in some of the spectra, the baseline features are as narrow as the spectral lines and could not be removed completely, resulting in negative features in the final spectra. Figure A.1 shows one input spectrum, the fitted spline, and the final spectrum. The gray box marks one of the narrow negative features in the spectrum.

The 291 GHz dataset was much less affected by bad baselines. The baselines were removed by fitting each spectrum with a 1st-order polynomial over the velocity ranges -120 – 120 km s^{-1} (20 km s^{-1} cloud), -70 – 120 km s^{-1} (50 km s^{-1} cloud), -90 – 120 km s^{-1} (G0.253+0.016, G0.411+0.050, G0.480–0.006), and -200 – 100 km s^{-1} (Sgr C, Sgr D).

2.3. H_2CO spectra

To obtain average spectra of the six H_2CO lines at 218 GHz and 291 GHz, we averaged the 218.15–218.85 GHz and 290.55–292.1 GHz emission, respectively, over the OTF map of each source. As an example, the spectra of the 20 km s^{-1} cloud and G0.411+0.050 are shown in Fig. 2. In addition to the six p- H_2CO lines in the two frequency ranges, we marked the transitions $\text{HC}_3\text{N}(24-23)$, $\text{CH}_3\text{OH}(4_{2,2}-3_{1,2})$, and o- $\text{H}_2\text{CO}(4_{3,2}-3_{3,1})$. The spectra of all sources are presented in Fig. B.1. To better compare the strength of the different lines, we chose the same intensity scale for all spectra.

The H_2CO emission at both frequencies is strongest in the 20 and 50 km s^{-1} clouds. Here, all six p- H_2CO lines are well-detected. In G0.411+0.050 and Sgr D, the H_2CO emission at 291 GHz is almost not detected in the average spectra.

In Fig. B.2, we overplot the $\text{H}_2\text{CO}(3_{0,3}-2_{0,2})$ and the $\text{H}_2\text{CO}(4_{0,4}-3_{0,3})$ spectra for the 20 and 50 km s^{-1} clouds. The figure shows that the line width of the two transitions is comparable.

2.4. Methanol contamination

The $\text{H}_2\text{CO}(3_{2,2}-2_{2,1})$ and the $\text{CH}_3\text{OH}(4_{2,2}-3_{1,2})$ transitions are separated by 35 MHz, corresponding to 25.5 km s^{-1} . These two lines are well-resolved and well-separated in our data. However, in sources for which the range of velocity components extends over more than 26 km s^{-1} , the integrated intensity maps of the $\text{H}_2\text{CO}(3_{2,2}-2_{2,1})$ line are contaminated by methanol emission for certain velocity components (see Fig. C.1). We thus excluded this line from the further analysis.

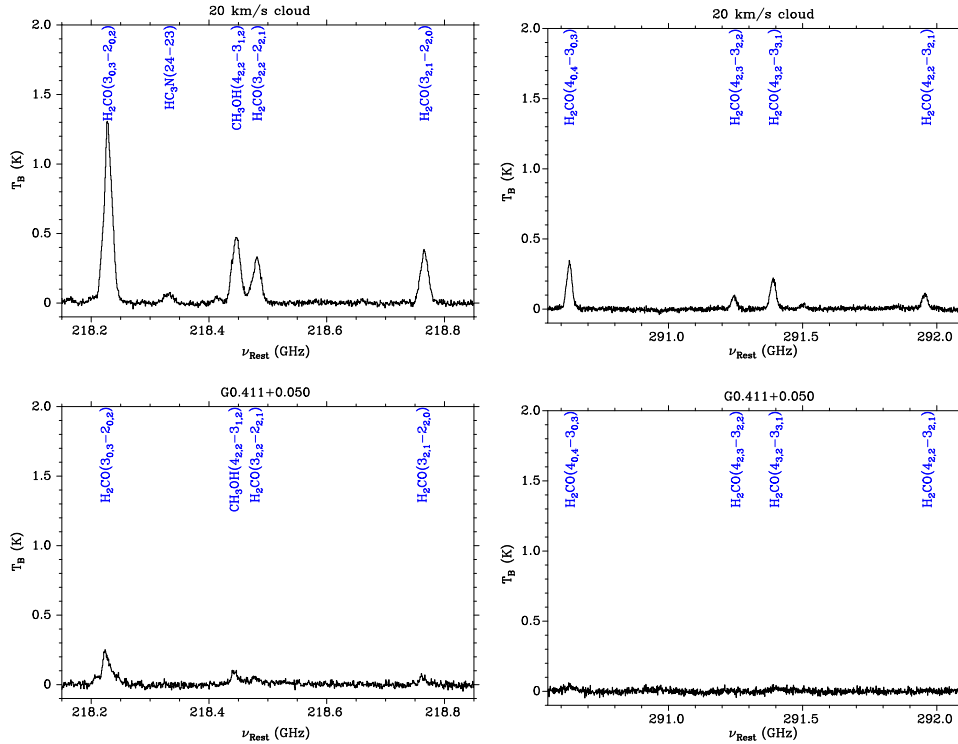


Fig. 2. Spectra of para- H_2CO transitions at 218 (left panels) and 291 GHz (right panels) of the 20 km s^{-1} cloud (upper panels) and G0.411+0.050 (lower panels), averaged over the whole OTF maps. Transitions of H_2CO , as well as other molecules are marked in the spectra.

3. Analysis

3.1. Velocity ranges

To determine the whole velocity range covered by H_2CO emission for each source, we used the 218 GHz spectra (Fig. B.1, Sect. 2.3) and zoomed in on the $\text{H}_2\text{CO}(3_{0,3}-2_{0,2})$ line. We fitted a linear baseline to line-free channels close to the line to obtain the average rms level in each OTF map. For each source, we determined the velocity range where the line emission was above 3σ (Col. 9 in Table 1, Fig. D.1). For Sgr C and Sgr D, we followed the same procedure but used the transition $\text{H}_2\text{CO}(4_{0,4}-3_{0,3})$.

To detect different velocity components, we subdivided the OTF maps into small tiles of size $33'' \times 33''$, slightly larger than the beam, and averaged the $\text{H}_2\text{CO}(3_{0,3}-2_{0,2})$ spectra over these areas. We fitted the line with several Gaussians if more than one velocity component was present and determined the central velocity of each component in each tile.

For each velocity component in each source, we averaged the $\text{H}_2\text{CO}(3_{0,3}-2_{0,2})$ spectra ($\text{H}_2\text{CO}(4_{0,4}-3_{0,3})$ in the case of Sgr C and Sgr D) over the area where this component dominated and again estimated the central velocity of the line in the averaged spectrum. To separate the components well, spatially and spectrally, in the following analysis, we set the velocity ranges over which the H_2CO emission is integrated as $\pm 3 \text{ km s}^{-1}$ around the central velocity of each component (Col. 10 in Table 1).

We detected velocity gradients in three of our clouds. In G0.253+0.016, the average velocities range from $\sim 40 \text{ km s}^{-1}$ in the south-west of the cloud to $\sim 0 \text{ km s}^{-1}$ in the North-East. We identified four spatially distinct velocity components at 0, 19, 39, and 78 km s^{-1} in this source. While the emission of the first three velocity components peaks towards the cloud, the emission of the 78 km s^{-1} component originates from the south-east

border of the cloud and might not be associated with this cloud.

In the 20 km s^{-1} cloud, the velocity gradient spreads over $\sim 30 \text{ km s}^{-1}$ from the south-east end of the cloud to the north-west part. The three velocity components we identified in this source are at 3, 11, and 30 km s^{-1} . Most of the 50 km s^{-1} cloud is at $\sim 45 \text{ km s}^{-1}$ but there are higher velocities detected at the north and lower velocities at the west end of the cloud. The velocity gradient also spans about $\sim 15 \text{ km s}^{-1}$. We could distinguish between two velocity components at 44 and 60 km s^{-1} .

We identified only one velocity component in the other clouds. The H_2CO emission peaks at 22 km s^{-1} in G0.411+0.050, 30 km s^{-1} in G0.480-0.006, -52 km s^{-1} in Sgr C, and -16 km s^{-1} in Sgr D.

3.2. Integrated intensity ratio and uncertainty maps

For each H_2CO transition in Table 2, we produced calibrated data cubes on a grid with a resolution of 1 km s^{-1} . The cubes are smoothed to a resolution of $33''$. The pixel size is $11''$. For each pixel of these cubes, we fitted linear baselines to line-free velocities at both sides of the lines. For each line and all velocity components of our targets, we produced maps of the uncertainty of the line intensity by assigning every pixel of the map the corresponding $\sigma(T_{\text{mb}})$ from the baseline fitting. The median of $\sigma(T_{\text{mb}})$ of the maps ranges between 35 and 59 mK per pixel at 218 GHz and 30 and 46 mK per pixel at 291 GHz (Cols. 7, 8 in Table 1).

As described in Sect. 1, the relative intensities of para- H_2CO lines yield estimates of the temperature and density of the gas.

We selected the following key line ratios:

$$R_{321} = \frac{\int I_{\text{H}_2\text{CO}(3_{2,1}-2_{2,0})} dv}{\int I_{\text{H}_2\text{CO}(3_{0,3}-2_{0,2})} dv} \Rightarrow \text{Temperature}$$

$$R_{422} = \frac{\int I_{\text{H}_2\text{CO}(4_{2,2}-3_{2,1})} dv}{\int I_{\text{H}_2\text{CO}(4_{0,4}-3_{0,3})} dv} \Rightarrow \text{Temperature}$$

$$R_{404} = \frac{\int I_{\text{H}_2\text{CO}(4_{0,4}-3_{0,3})} dv}{\int I_{\text{H}_2\text{CO}(3_{0,3}-2_{0,2})} dv} \Rightarrow \text{Density.}$$

For a better readability of the paper, we will abbreviate these ratios to R_{321} , R_{404} , and R_{422} , respectively, in the following text.

For each pixel in the data cubes, we integrated the emission of the para- H_2CO lines independently over the same velocity range v_{range} , yielding separate integrated intensity maps for the different lines. We produced these maps for all velocity components of our targets (v_{range} in Cols. 9, 10 in Table 1; Figs. E.1–E.7).

We identified the pixels in the OTF maps of each source where the integrated emission of the $\text{H}_2\text{CO}(3_{0,3}-2_{0,2})$ and the $\text{H}_2\text{CO}(4_{0,4}-3_{0,3})$ lines, respectively, was above the $5 \cdot \sigma(T_{\text{mb}}) \cdot \sqrt{\frac{v_{\text{range}}}{\Delta v_{\text{res}}}} \cdot \Delta v_{\text{res}}$ threshold. The parameter Δv_{res} is the velocity resolution of our data. For these pixels, we determined the aforementioned ratios from the integrated intensity maps of these lines, yielding integrated intensity ratio maps (Figs. F.1–F.7).

For positions where the integrated emission of the line in the numerator was below the 5σ threshold, the integrated intensity value was exchanged for the value $5 \cdot \sigma(T_{\text{mb}}) \cdot \sqrt{\frac{v_{\text{range}}}{\Delta v_{\text{res}}}} \cdot \Delta v_{\text{res}}$, representing upper limits of the ratios (marked with Xs in the maps). For each pixel in the ratio maps (except upper limits), we then determined the uncertainty of the ratio via Gaussian error propagation, using the uncertainty maps of the intensity of the two corresponding lines. The remaining pixels (corresponding to the pixels with upper limits in the ratio maps) were blanked in gray. In two velocity components of two sources, all or almost all pixels are upper limits (G0.253+0.016: 16–22 km s⁻¹, 291 GHz; 75–81 km s⁻¹, 218 and 291 GHz; G0.411+0.050: both velocity components, 291 GHz).

4. Modeling

4.1. Fundamental approach

We use RADEX (van der Tak et al. 2007) and a related solver (Fujun Du’s myRadex³) to create model intensities for the para- H_2CO lines. The calculations are executed using pyradex, a Python-based wrapper for RADEX (developed by A. Ginsburg⁴). The collision rates used here (from Wiesenfeld & Faure 2013) are retrieved from the LAMDA database (Schöier et al. 2005). This approach is conceptually identical to the one employed by Ginsburg et al. (2016), though we choose slightly different gas properties to solve the radiative transfer problem.

We adopt a fiducial set of conditions for our calculations of emission line intensities and ratios. Below we show that our temperature estimates are robust with respect to the choice of values for these parameters. We assume H_2 particle densities of 10^5 cm^{-3} . This choice is motivated by the average densities

of a few 10^4 cm^{-3} as estimated for our targets via the analysis of dust emission maps (Kauffmann et al. 2016). The column density of para- H_2CO is set to $5 \times 10^{13} \text{ cm}^{-2}$. For a representative H_2 column density of $5 \times 10^{22} \text{ cm}^{-2}$ (Kauffmann et al. 2016) this corresponds to an abundance of 10^{-9} with respect to H_2 , a value that is suggested by previous work (for a summary, see Ginsburg et al. 2016). We adopt a velocity dispersion of 5 km s^{-1} . This value is appropriate for structures with a radius of order 1 pc, which is about the diameter of our beam. The calculations are executed assuming a spherical geometry.

We compute the intensities of para- H_2CO emission lines under the aforementioned conditions. These intensities can be used to calculate the R_{321} and R_{422} line ratios. These line ratios are known to be highly sensitive to the temperature while being rather insensitive to changes in other parameters (e.g. Mangum & Wootten 1993, see left panel of Fig. 3 for R_{321}). This trend is confirmed in calculations discussed below. For this reason, the R_{321} and R_{422} line ratios can be used to estimate the kinetic gas temperature.

In essence, we use the aforementioned RADEX calculations for kinetic gas temperatures of 10 to 300 K to obtain functions that yield estimates of the kinetic gas temperature for given R_{321} or R_{422} . The ratios range from 0 to values larger than 0.5 for this temperature range. The resulting function for R_{321} is almost identical to the one used by Ginsburg et al. (2016). This is in particular remarkable because Ginsburg et al. use large velocity gradient (LVG) calculations, while we choose to adopt spherical model geometries. Here, we opt for the latter modeling geometry since it is close to the naive picture of a cloud with a well-defined boundary that is immersed in tenuous material. The comparison with the LVG case shows, however, that our analysis is robust with respect to the adopted modeling geometry.

4.2. Systematic uncertainties

We assess the robustness of this method by repeating the line ratio calculations for different choices in gas properties. We vary the velocity dispersion between 2 and 10 km s^{-1} , increase and decrease in column density by a factor of 10, explore lower densities of 10^4 cm^{-3} , and examine the results for the slab and LVG models available within RADEX (Fig. G.1). This shows that, for a given line ratio, none of these modifications lead to temperatures that deviate by more than $\pm 30\%$ from the result obtained using our fiducial case (see Fig. G.1). For reference, we note that spherical model geometries give the lowest temperatures, followed by slightly elevated values for LVG conditions. Slab geometries, however, give, for a fixed line ratio, temperatures that are up to 30% higher than those found for the fiducial case. We note in particular that these calculations explore the density range between 10^4 and 10^5 cm^{-3} that is suggested by the observations of dust emission discussed by Kauffmann et al. (2016). Variations in density by a factor 10 have no significant impact on our results.

In the high column density Galactic center environment, the $\text{H}_2\text{CO}(3_{0,3}-2_{0,2})$ emission might be optically thick. This saturation would cause a falsely high R_{321} line ratio in our integrated intensity ratio maps. A higher ratio implies higher temperatures. Thus, an optically thick $\text{H}_2\text{CO}(3_{0,3}-2_{0,2})$ line would mimic higher gas temperatures in the clouds.

We have executed more detailed experiments for selected positions to understand the impact of the line optical depth. For example, we modeled the emission from the 20 km s^{-1} cloud in the velocity slice of 8 to 14 km s^{-1} (Fig. G.2, left panel). The $3_{0,3}-2_{0,2}$ transition has a velocity-integrated peak intensity of

³ <https://github.com/fjdu/myRadex>

⁴ <https://github.com/keflavich/pyradex>

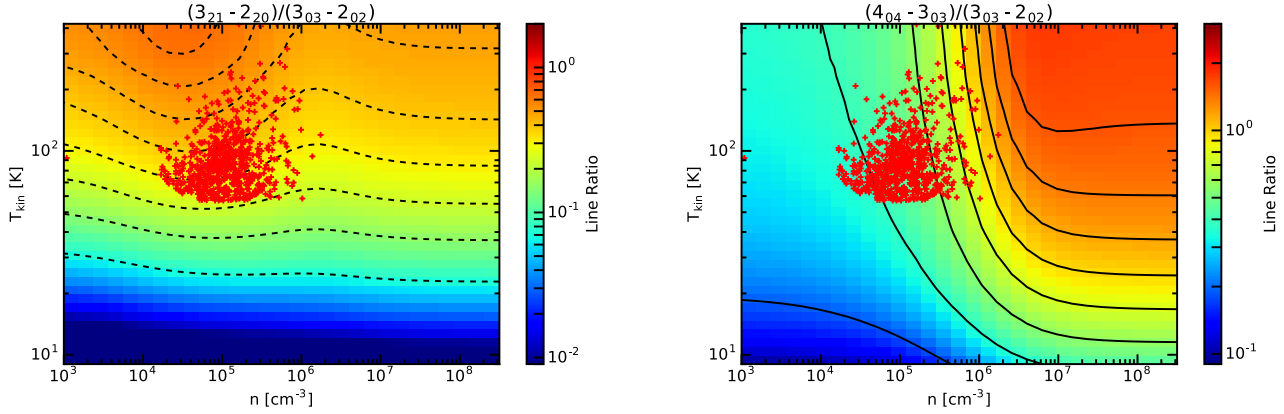


Fig. 3. *Left:* R_{321} as a function of kinetic temperature T_{kin} and density n . The plot shows that the ratio is mostly dependent on temperature and independent of the density of the gas. *Right:* R_{404} as a function of kinetic temperature T_{kin} and density n . The plot shows the strong dependence of the ratio on both temperature and density for densities $< 10^7 \text{ cm}^{-3}$. The red plus signs indicate locations where the observed line ratios R_{321} and R_{404} are matched at the same time.

15 K km s^{-1} (blue line in top panel of Fig. G.2). At this peak position the $4_{0,4}-3_{0,3}$ transition has an integrated intensity of 4 K km s^{-1} (blue line in bottom panel of Fig. G.2), while we find $R_{321} = 0.25$ and $R_{422} = 0.35$ (red line in top and bottom panel, respectively, of Fig. G.2). Further, the analysis of dust emission maps (Kauffmann et al. 2016) indicates H_2 densities below 10^5 cm^{-3} . This limits the parameter space explored in our radiative transfer experiments. In our modeling, we thus require that the model intensities match the observed ones for H_2 densities below 10^5 cm^{-3} . For these constraints we find that the data for the transitions near 218 GHz can only be matched if we increase the column density to a multiple of the fiducial value (Fig. G.2, right panel, for an increased column density of $5 \times 10^{14} \text{ cm}^{-2}$). The optical depth of the $3_{0,3}-2_{0,2}$ line is larger than one under these conditions. One might think that the high optical depth leads to massive biases in temperature estimates. This is, however, not the case: given a fixed line ratio, conditions with high optical depth can imply temperatures lower by 30% for optical depths $\gtrsim 5$ (i.e. our procedure, which assumes low optical depth, overestimates gas temperatures in regions of high optical depth).

4.3. Observational uncertainties

Further uncertainties in the temperature result from observational uncertainties in line ratios due to noise. To handle these uncertainties, we first obtain two additional temperature estimates per map position. These two estimates are calculated for line ratios that are equal to the observed value plus or minus the observed uncertainty in the line ratio. Conceptually these values bracket the range of possible temperatures for a given map position. The difference between these values represents the change in kinetic gas temperatures when changing the line ratio by twice its uncertainty (i.e. from $R_i - \sigma[R_i]$ to $R_i + \sigma[R_i]$, where R_i and $\sigma[R_i]$ are the line ratio and its uncertainty). Half of this difference can thus be considered to represent the average temperature uncertainty associated with a line ratio uncertainty $\pm\sigma(R_i)$. In our analysis, we thus calculate for every map position the temperatures corresponding to $R_i \pm \sigma[R_i]$, and we report half of the difference between these temperatures as the observational uncertainty in kinetic gas temperatures. We are aware that the temperature uncertainties are asymmetric around the temperature

value. However, we decided that the chosen method is the best way to present the uncertainties in this paper.

For some locations, the observations only yield upper limits to the line ratios. In such cases we take this upper limit to R_i , we calculate the associated temperature, and we report this resulting value as an upper limit to the kinetic gas temperature.

5. Discussion

The temperature maps of all velocity components of all sources are shown in Figs. H.1–H.7. Upper limits in the temperature maps are marked again with Xs. The corresponding pixels in the uncertainty maps are blanked in white. The measured temperatures range between 28 and 242 K at 218 GHz and between 37 and 252 K at 291 GHz (excluding upper limit values of the temperature). This shows that the gas temperatures are everywhere in the clouds much higher than the dust temperatures that are measured towards these clouds ($\sim 25 \text{ K}$, Molinari et al. 2011). However, temperatures above $\sim 150 \text{ K}$ have to be considered as lower limits since the radiative transfer models start to diverge significantly at these temperatures and the para- H_2CO line ratios are intrinsically insensitive to higher temperatures (Mangum & Wootten 1993; Ginsburg et al. 2016).

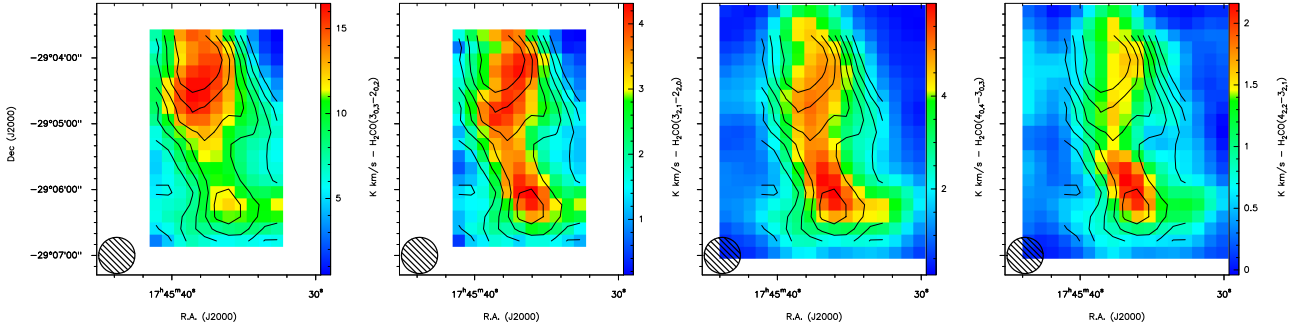
We present the different plots we generated (integrated intensity maps, line ratio and uncertainty maps, temperature and uncertainty maps) for the $8-14 \text{ km s}^{-1}$ component of the 20 km s^{-1} cloud in Fig. 4. In the last panel, we show a three-color image of *Spitzer*/GLIMPSE data (Churchwell et al. 2009, blue = $3.6 \mu\text{m}$, green = $4.5 \mu\text{m}$, red = $8.0 \mu\text{m}$) of this source.

5.1. Average temperatures

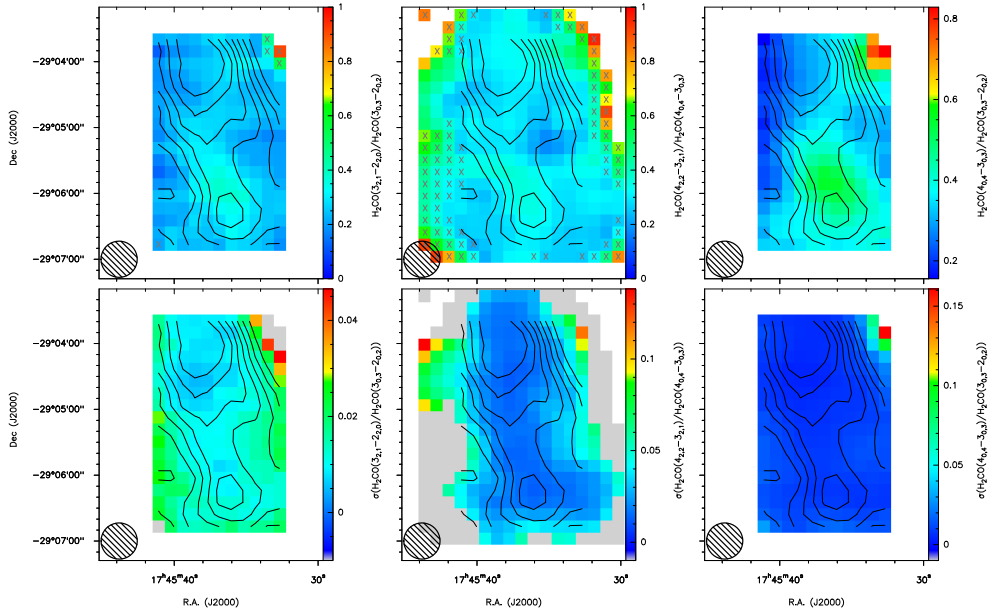
To estimate and compare the overall temperatures of the clouds, we determined the weighted average of the temperature in each cloud for each velocity component, first, derived from the 218 GHz lines and, second, from the 291 GHz ladder. The squared reciprocal of the temperature uncertainties served as the weights. In this calculation, temperature upper limits were not included. The results are listed in Table 3. In addition, we give the minimal and maximal temperature of each map in the table.

In most cases, the average temperature derived from the 291 GHz data is higher than the average temperature derived from the 218 GHz lines but the values agree within the

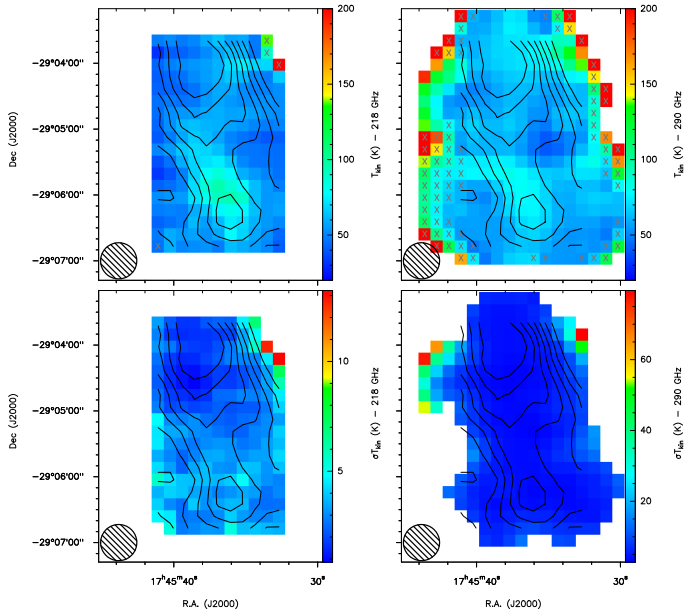
H₂CO integrated intensity maps (from left to right: H₂CO(3_{0,3}–2_{0,2}), H₂CO(3_{2,1}–2_{2,0}), H₂CO(4_{0,4}–3_{0,3}), and H₂CO(4_{2,2}–3_{2,1}))



H₂CO ratio (upper panels) and uncertainty maps (lower panels) (from left to right: R_{321} , R_{422} , and R_{404}).



H₂CO temperature (upper panels) and uncertainty maps (lower panels), derived from the 218 GHz (left panels) and 291 GHz data (right panels)



Spitzer/GLIMPSE RGB image (blue = 3.6 μ m, green = 4.5 μ m, and red = 8.0 μ m)

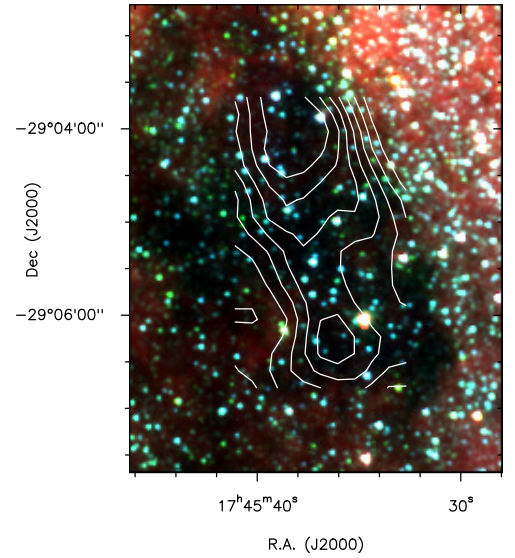


Fig. 4. Summary of the produced maps for the 8–14 km s⁻¹ component of the 20 km s⁻¹ cloud. The contours show the moment 0 map of the H₂CO(3_{0,3}–2_{0,2}) transition, produced over the whole velocity range of the source (levels: 30–90% of the maximum in steps of 10%). The circle in the lower left corner shows the 33'' beam.

Table 3. Minimal T_{Min} , maximal T_{Max} , and weighted average T_{Average} temperatures, as well as 1σ uncertainties of the weighted average temperature for all temperature maps (i.e. each source, each velocity component, and each frequency).

Source	Velocity component (km s ⁻¹)	218 GHz				291 GHz				T_{Ginsburg} (K)
		T_{Min} (K)	T_{Average} (K)	σ_{Average} (K)	T_{Max} (K)	T_{Min} (K)	T_{Average} (K)	σ_{Average} (K)	T_{Max} (K)	
20 km s ⁻¹ cloud	-15-36	28	58	16	133	37	62	11	163	64
	0-6	36	70	16	183	43	71	9	115	
	8-14	31	54	10	96	40	62	9	191	
	27-33	31	48	11	93	45	62	13	199	
50 km s ⁻¹ cloud	16-80	30	82	29	242	41	82	14	223	91
	41-47	44	87	18	142	53	91	15	150	
	57-63	38	56	12	115	71	109	21	252	
	-6-54	29	50	14	203	41	61	12	212	
G0.253+0.016	-3-3	61	81	16	180	56	77	17	140	82
	16-22	38	49	11	222	76	90	14	111	
	36-42	42	72	21	189	47	69	16	210	
G0.411+0.050	75-81	72	72		72	95	109	25	183	57
	10-30	41	49	8	132					
G0.480-0.006	19-25	49	59	11	197					84
	19-44	32	40	8	117	50	69	18	239	
Sgr C	27-33	42	56	12	161	65	84	14	189	53
	-60--46					54	72	8	173	
Sgr D	-55--49					43	59	7	191	52
	-17--14					47	56	8	80	
	-19--13					39	50	7	66	

Notes. The last column gives the average temperature of each source from the survey of Ginsburg et al. (2016).

1σ temperature uncertainty. In two cases, however, the temperature difference is rather large (50 km s⁻¹ cloud: 57–63 km s⁻¹ component, G0.253+0.016: 16–22 km s⁻¹ component). In Fig. H.8, we visualize these results in temperature box plots.

To check the validity of our results, we compared our temperature measurements to the H₂CO 218 GHz survey of Ginsburg et al. (2016). For each source, we averaged their temperature map (their Fig. 7c) over the sizes of our 218 GHz OTF maps (the 291 GHz OTF maps for Sgr C and Sgr D). The obtained values are shown in the last column of Table 3. These average temperatures are roughly consistent with our results, except for G0.480–0.006. Here, the average temperature of Ginsburg et al. (2016) is much higher than our values at 218 GHz. However, our 291 GHz measurements do show a high temperature component. We conclude that, on average, our study yields similar temperatures for the observed clouds as the survey of Ginsburg et al. (2016).

Comparing the average temperature of the whole velocity range of each source, we noticed a large spread of temperatures between 40 K in G0.480–0.006 and 82 K in the 50 km s⁻¹ cloud. There is no clear correlation of the average temperature with the location of the clouds in the CMZ.

5.2. Temperature gradients within clouds

Table 3 shows that the average temperatures of the different velocity components in the sources are not the same. Differences of ~30 K are observed. This indicates the presence of temperature gradients in the sources. These results show that averaging the temperatures over the whole velocity range of the clouds can yield misleading values of the temperature. It is thus important to look at the temperatures of the gas with different velocities to understand the underlying temperature structures of the clouds.

The 20 km s⁻¹ cloud and G0.253+0.016 even show temperature gradients across the sources within one velocity component. In Fig. 4, the temperature map of the 8–14 km s⁻¹ component of the 20 km s⁻¹ cloud is plotted. There is a clear temperature gradient from ~60–70 K at the north-east side of the cloud to ~110–120 K in the southern part. A similar gradient is seen in the 36–42 km s⁻¹ component of G0.253+0.016 (Fig. H.3, fourth panel), with the temperature increasing from ~70 K in the north of the cloud to more than 150 K in the southern part.

In a forthcoming paper, we will compare the temperature structures of the clouds with tracers of shocks (e.g. observations of SiO, Class I methanol masers) or star formation (Class II methanol masers, water masers) to apprehend the cause for the different temperatures.

5.3. Evidence for heating by turbulence

To better understand the temperature structures in our clouds, we investigate the energy balance in the gas following the analysis of Ginsburg et al. (2016). We do not consider stellar heating or energy injection through supernovae since these processes can only explain local heating of the clouds, but not their overall high gas temperature. Ao et al. (2013) already excluded diffuse X-rays as the main heating source, leaving only cosmic ray and mechanical heating (turbulence) as the energetically important heating processes. Ginsburg et al. (2016) concluded that cosmic ray heating is either irrelevant in the CMZ or the heating is non-uniform since uniform heating cannot simultaneously explain the high (>100 K) and low (<50 K) temperatures measured in the CMZ. The detected temperature gradients in our clouds also exclude the latter, except if the cosmic ray heating is non-uniform on very small scales (~1 pc). We will produce similar gas temperature vs. line width plots (as their Fig. 9) for the 218 and 291 GHz temperatures and compare our data to the same models

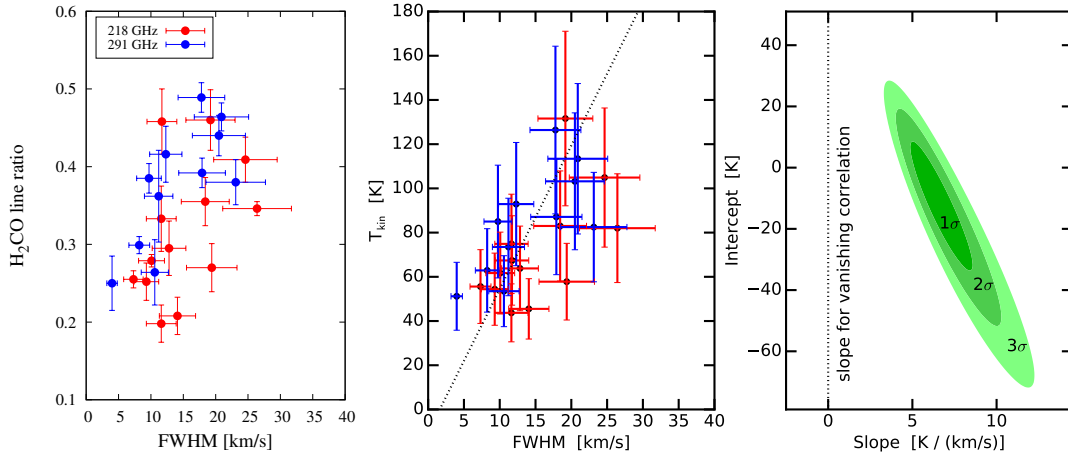


Fig. 5. *Left and middle panels:* correlation plots of H₂CO integrated intensity ratio and kinetic temperature, respectively vs. line width. The error bars present the standard deviation of the weighted average for the integrated intensity ratio, 20% uncertainty in the line width and 30% uncertainty in the temperature. The best linear fit to the temperature data using the total least-square method (Vanderplas et al. 2012) is shown as the solid line. *Right panel:* The possible slope and intercept values with the 1, 2, and 3 σ likelihood contours.

as used in Ginsburg et al. (2016) to narrow down the parameter space of possible heating models.

To collect the data of these plots, we chose one or several positions in the 218 and 291 GHz temperature maps of the 6 km s⁻¹ broad velocity components of each source where none of the pixels in a 33'' \times 33'' tile (roughly corresponding to the size of the beam) around these positions are upper limits. The boxes are overlaid on the temperature maps in Figs. H.1–H.7. We then determined the weighted average temperature within these boxes, using the squared reciprocal of the temperature uncertainties as weights. Averaging the H₂CO(3_{0,3}–2_{0,2}) spectra of the nine pixels in the boxes, we fitted the line with one or more velocity components depending on the source. We then assigned each average temperature value the line width of the corresponding velocity component. We excluded the 20 km s⁻¹ cloud from this analysis because we could not fit the line width of the different components unambiguously. To make sure that any trend we see is real and not due to the radiative transfer modeling, we also obtained the average line ratios R_{321} and R_{422} in those tiles. The values for line ratio, temperature, and line width are listed in Table I.1. In Fig. 5, we show the relation of line ratio (left panel) and temperature (middle panel), respectively, versus line width.

Considering the statistical uncertainties associated with both parameters (20% for the line width, 30% for the temperature), we adopt the method of total least squares (Vanderplas et al. 2012) to measure the slope of the $dv - T_{\text{kin}}$ relation. Since we are integrating the emission of the H₂CO lines over a fixed velocity range, it is safe to assume that the temperature and line width measurements are uncorrelated, so we set the covariance between them to be zero. Figure 5 shows a statistically significant positive correlation, which suggests that regions of higher line widths in our clouds are expected to have higher gas temperature. This implies that turbulence might play a direct role in gas heating.

Figure 6 shows a collection of thermal equilibrium models computed using the DESPOTIC (Krumholz 2014) code. Each model uses the heating terms specified in the legend and both line and dust cooling. The models compute the equilibrium temperature achieved at the specified density. The primary variable being varied is the line width, which is treated as an observational proxy for the 3D velocity dispersion following the

equation $\sigma_{3D} = \sqrt{3}\sigma_{1D}$. In contrast with Ginsburg et al. (2016), who observed a wider range in densities and environments, our data show a strong trend between the observed temperature and the velocity dispersion. These are readily explained by the $n = 10^5$ cm⁻³ model that assumes that each cloud has a line-of-sight length of 1 pc. These observations therefore significantly strengthen the case put forth by Ao et al. (2013) and Ginsburg et al. (2016) that the densest Galactic center clouds are predominantly heated by turbulence.

5.4. Density constraints

Following Mangum & Wootten (1993), the integrated intensity ratio of H₂CO $\Delta J = 1$ lines with different J , but the same K_a quantum numbers constrains the density of the gas. Figure 3 (right panel) shows that the R_{404} ratio depends strongly on both temperature and density for densities $< 10^7$ cm⁻³, while the R_{321} ratio only depends on temperature (Fig. 3, left panel). Thus, combining the measurements of the R_{321} and R_{422} ratios that yield the temperature with the R_{404} ratio, we can estimate the density in the clouds. The red plus signs in Fig. 3 show the locations where the R_{321} and R_{404} ratios are matched at the same time. Due to the significant dependence of the density estimate on the temperature estimate and our temperature uncertainties of $\sim 30\%$, we cannot compute density maps of our clouds. However, we constrain the density of the widespread warm gas in our clouds to 10^4 – 10^6 cm⁻³. Efforts are ongoing to further constrain this range using the cm transitions of H₂CO (Ginsburg et al., in prep.).

6. Conclusion

In this paper, we present H₂CO observations of five and seven CMZ clouds at 218 and 291 GHz, respectively. Combining integrated intensity H₂CO line ratios with radiative transfer models, we obtain gas temperature maps for our clouds. The two different sets of H₂CO lines (H₂CO(3–2) at 218 GHz and H₂CO(4–3) at 291 GHz) yield two independent estimates of the gas temperature.

Our observations at 218 GHz are a factor of ~ 1.5 deeper than previous H₂CO CMZ observations by Ginsburg et al. (2016,

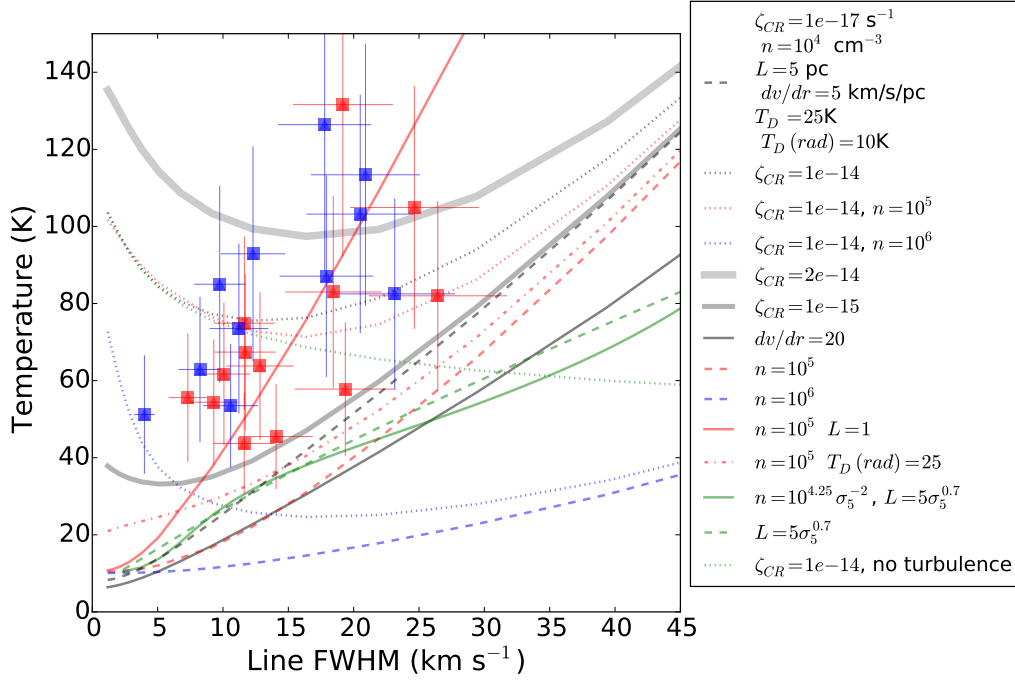


Fig. 6. Temperature versus line width plot, overlaid with thermal equilibrium models computed using the DESPOTIC (Krumholz 2014) code (see also Fig. 9 of Ginsburg et al. 2016). The data is consistent with the $n = 10^5 \text{ cm}^{-3}$ model.

compare our median rms values of ~ 45 mK per pixel to their noise level of 70 mK per pixel). While Ginsburg et al. focus on the global temperature differences in the CMZ, we disentangle the different velocity components of the gas in our sources and investigate their temperature structures. This is a significant step since the CMZ clouds exhibit the widest velocity components observed in our galaxy.

From a comparison of the H_2CO main lines at 218 and 291 GHz, we accessed that the $\text{H}_2\text{CO}(3_{0,3}-2_{0,2})$ line is optically thick in some parts of the clouds. Combining the observed line ratios R_{321} and R_{404} , we constrain the density of the warm cloud gas to $10^4-10^6 \text{ cm}^{-3}$.

Our temperature maps at 218 and 291 GHz show clear temperature gradients in our clouds. This indicates that heating mechanisms that act on the bulk of the molecular gas cannot be the main heating sources. Cosmic ray heating is only possible if the heating is non-uniform on very small scales. In a following paper, we will compare our results with complementary observations of shock and star formation tracers, as well as supernova remnants in the clouds to understand if these gradients are caused by local heating through cloud collisions, feedback from new born stars, or the explosion of stars.

Comparing the line widths of the main H_2CO lines at 218 and 291 GHz with the measured temperatures at selected positions in our clouds, we found a clear positive correlation between these two parameters. This indicates that turbulence plays an important role in the heating of the gas. Our data is consistent with a turbulence model with a density $n = 10^5 \text{ cm}^{-3}$ that assumes that each cloud has a line-of-sight length of 1 pc.

Acknowledgements. We thank the APEX team and MPIFR observers for carrying out these service-mode observations. The authors are thankful for the helpful comments of the anonymous referee. T.P. acknowledges support from the Deutsche Forschungsgemeinschaft, DFG via the SPP (priority program) 1573 Physics of the ISM. This research has made use of NASA's Astrophysics Data System Bibliographic Services.

References

- Ao, Y., Henkel, C., Menten, K. M., et al. 2013, *A&A*, **550**, A135
Blum, R. D., Damiani, A., & Conti, P. S. 1999, *AJ*, **117**, 1392
Churchwell, E., Babler, B. L., Meade, M. R., et al. 2009, *PASP*, **121**, 213
Ginsburg, A., Henkel, C., Ao, Y., et al. 2016, *A&A*, **586**, A50
Güsten, R., Walmsley, C. M., & Pauls, T. 1981, *A&A*, **103**, 197
Güsten, R., Nyman, L. Å., Schilke, P., et al. 2006, *A&A*, **454**, L13
Heyminck, S., Kasemann, C., Güsten, R., de Lange, G., & Graf, U. U. 2006, *A&A*, **454**, L21
Hüttmeister, S., Wilson, T. L., Bania, T. M., & Martin-Pintado, J. 1993, *A&A*, **280**, 255
Immer, K., Schuller, F., Omont, A., & Menten, K. M. 2012, *A&A*, **537**, A121
Kauffmann, et al. 2016, submitted
Klein, B., Hochgürtel, S., Krämer, I., et al. 2012, *A&A*, **542**, L3
Klein, T., Ciechanowicz, M., Leinz, C., et al. 2014, *IEEE Transactions on Terahertz Science and Technology*, **4**, 588
Kruijssen, J. M. D., & Longmore, S. N. 2013, *MNRAS*, **435**, 2598
Krumholz, M. R. 2014, *MNRAS*, **437**, 1662
Lis, D. C., Li, Y., Dowell, C. D., & Menten, K. M. 1999, in *The Universe as Seen by ISO*, eds. P. Cox, & M. Kessler, *ESA SP*, **427**, 627
Longmore, S. N., Bally, J., Testi, L., et al. 2013, *MNRAS*, **429**, 987
Mangum, J. G., & Wootten, A. 1993, *ApJS*, **89**, 123
Mehring, D. M., Goss, W. M., Lis, D. C., Palmer, P., & Menten, K. M. 1998, *ApJ*, **493**, 274
Mills, E. A. C., & Morris, M. R. 2013, *ApJ*, **772**, 105
Molinari, S., Bally, J., Noriega-Crespo, A., et al. 2011, *ApJ*, **735**, L33
Morris, M., & Serabyn, E. 1996, *ARA&A*, **34**, 645
Ott, J., Weiß, A., Staveley-Smith, L., Henkel, C., & Meier, D. S. 2014, *ApJ*, **785**, 55
Pety, J. 2005, in *SF2A-2005: Semaine de l'Astrophysique Française*, eds. F. Casoli, T. Contini, J. M. Hameury, & L. Pagani (Les Ulis: EDP Sciences), 721
Sawada, M., Tsujimoto, M., Koyama, K., et al. 2009, *PASJ*, **61**, S209
Schöier, F. L., van der Tak, F. F. S., van Dishoeck, E. F., & Black, J. H. 2005, *A&A*, **432**, 369
Schuller, F., Menten, K. M., Contreras, Y., et al. 2009, *A&A*, **504**, 415
Shirley, Y. L. 2015, *PASP*, **127**, 299
van der Tak, F. F. S., Black, J. H., Schöier, F. L., Jansen, D. J., & van Dishoeck, E. F. 2007, *A&A*, **468**, 627
Vanderplas, J., Connolly, A., Ivezić, Ž., & Gray, A. 2012, in *Proc. Conference on Intelligent Data Understanding (CIDU)*, 47
Vassilev, V., Meledin, D., Lapkin, I., et al. 2008, *A&A*, **490**, 1157
Wiesenfeld, L., & Faure, A. 2013, *MNRAS*, **432**, 2573
Yusef-Zadeh, F., Hewitt, J. W., Arendt, R. G., et al. 2009, *ApJ*, **702**, 178

Appendix A: Calibration

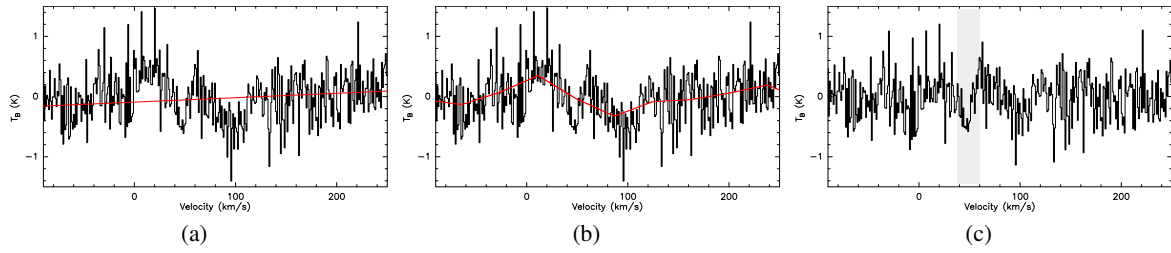


Fig. A.1. Example spectra of the $\text{H}_2\text{CO}(3_{0,3}-2_{0,2})$ transition of target G0.253+0.016 to show the spline-fitting of bad baselines. *Left:* input spectrum showing a bad baseline. The red line shows a linear baseline for comparison. *Middle:* input spectrum with the spline spectrum (red) overlaid. *Right:* baseline-subtracted spectrum. The gray box shows a baseline feature that was not removed in the spline-fitting due to its narrow width.

Appendix B: Spectra

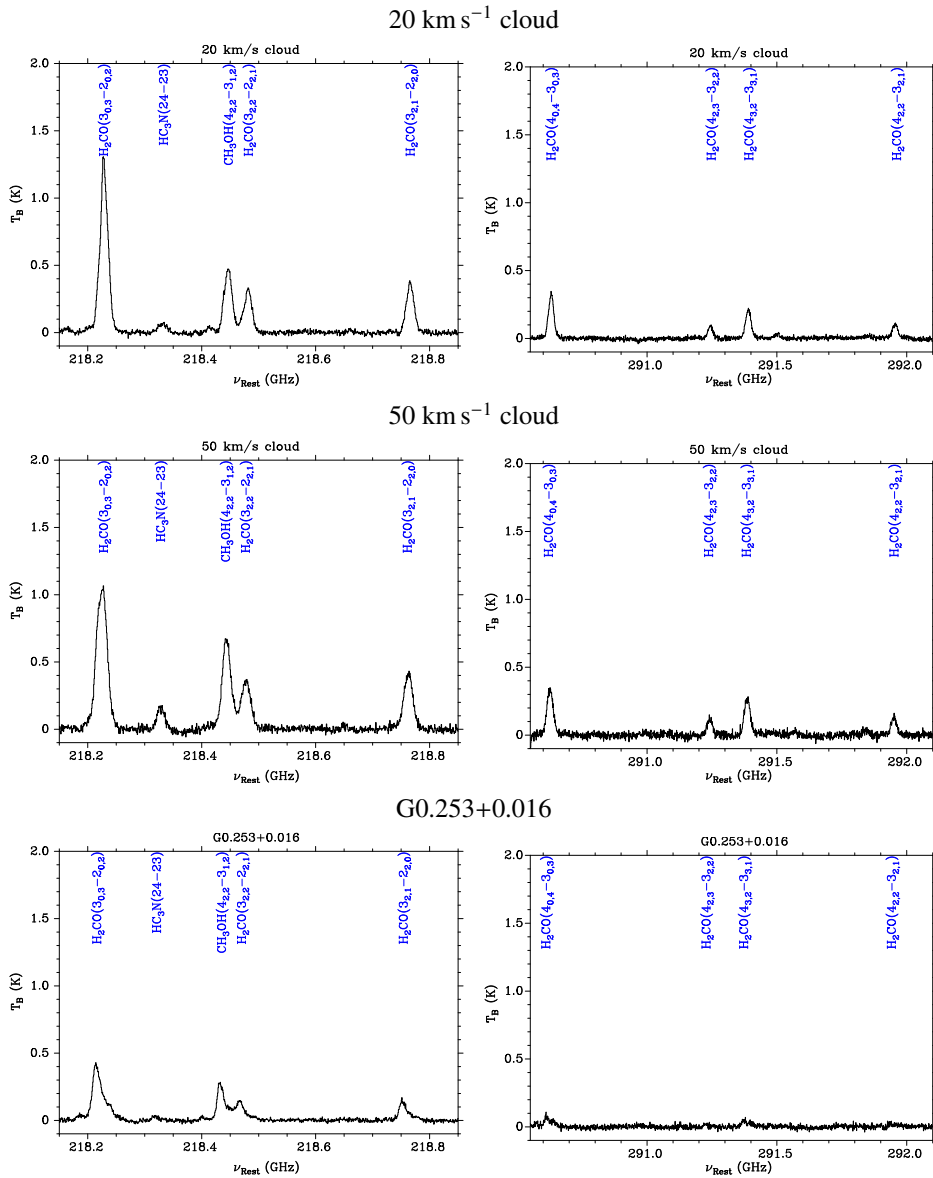
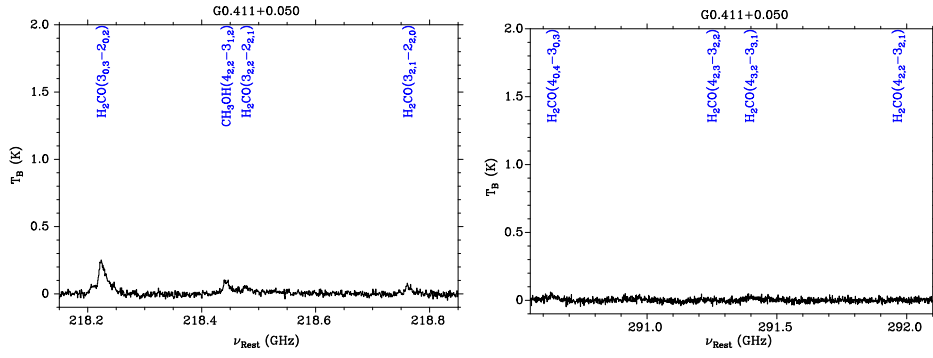
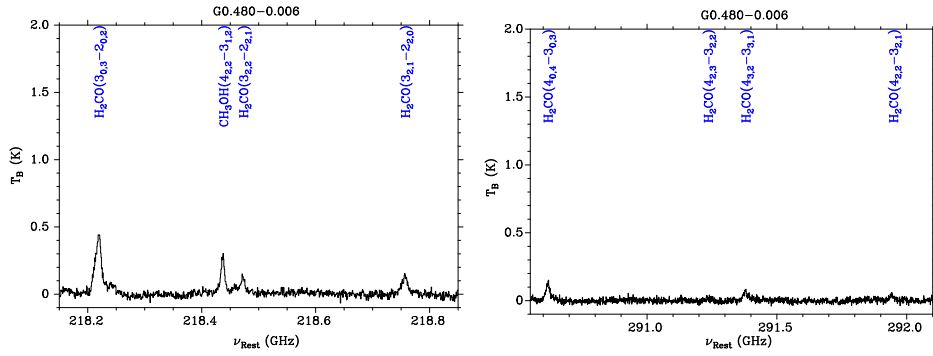


Fig. B.1. Spectra of para- H_2CO transitions at 218 (*left panels*) and 291 GHz (*right panels*), averaged over the whole OTF map of each source. H_2CO as well as other lines are marked in the spectra.

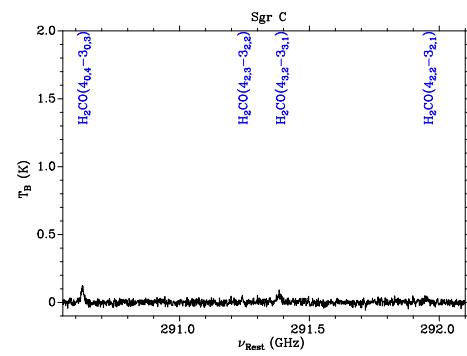
G0.411+0.050



G0.480-0.006



Sgr C



Sgr D

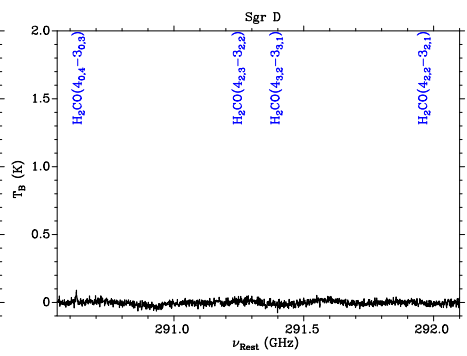


Fig. B.1. continued.

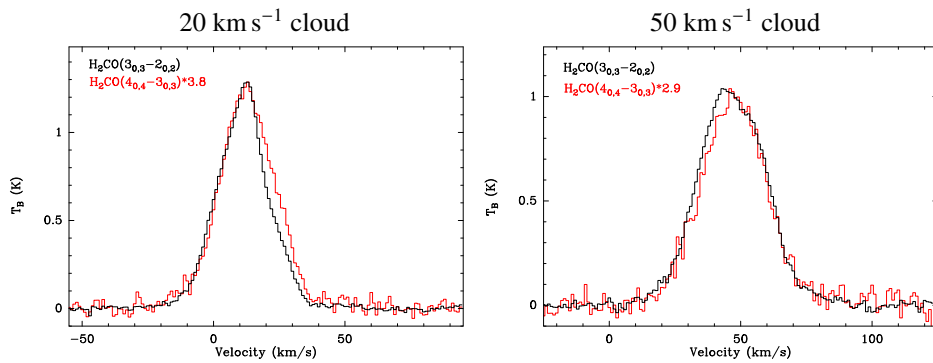


Fig. B.2. The spectra of the $\text{H}_2\text{CO}(3_{0,3}-2_{0,2})$ and $\text{H}_2\text{CO}(4_{0,4}-3_{0,3})$ transitions for the 20 km s^{-1} cloud (left) and the 50 km s^{-1} cloud (right) plotted on top of each other. The spectra of $\text{H}_2\text{CO}(4_{0,4}-3_{0,3})$ were multiplied by a factor of 3.8 and 2.9 in the left and right panels, respectively, to bring the two lines to the same scale. The plots show that the two transitions have comparable width in both sources.

Appendix C: Methanol contamination

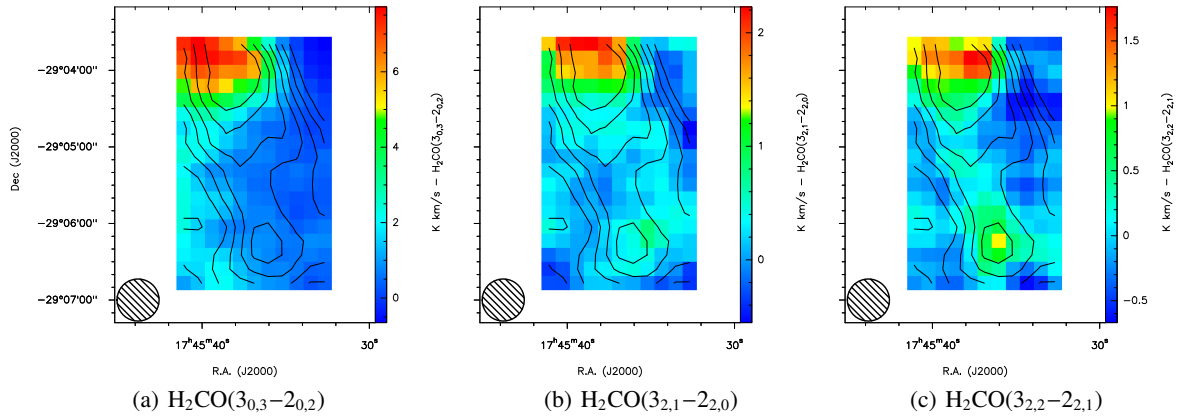


Fig. C.1. Comparison of the integrated emission of $\text{H}_2\text{CO}(3_{0,3}-2_{0,2})$, $\text{H}_2\text{CO}(3_{2,1}-2_{2,0})$ and $\text{H}_2\text{CO}(3_{2,2}-2_{2,1})$ of the 20 km s^{-1} cloud over the velocity range $27-33 \text{ km s}^{-1}$, showing the contamination of the $\text{H}_2\text{CO}(3_{2,2}-2_{2,1})$ line with methanol emission at the south of the cloud. The contours show the moment 0 map of the $\text{H}_2\text{CO}(3_{0,3}-2_{0,2})$ transition, produced over the whole velocity range of the source (levels: 30–90% of the maximum in steps of 10%) The circle in the *lower left corner* shows the $33''$ beam.

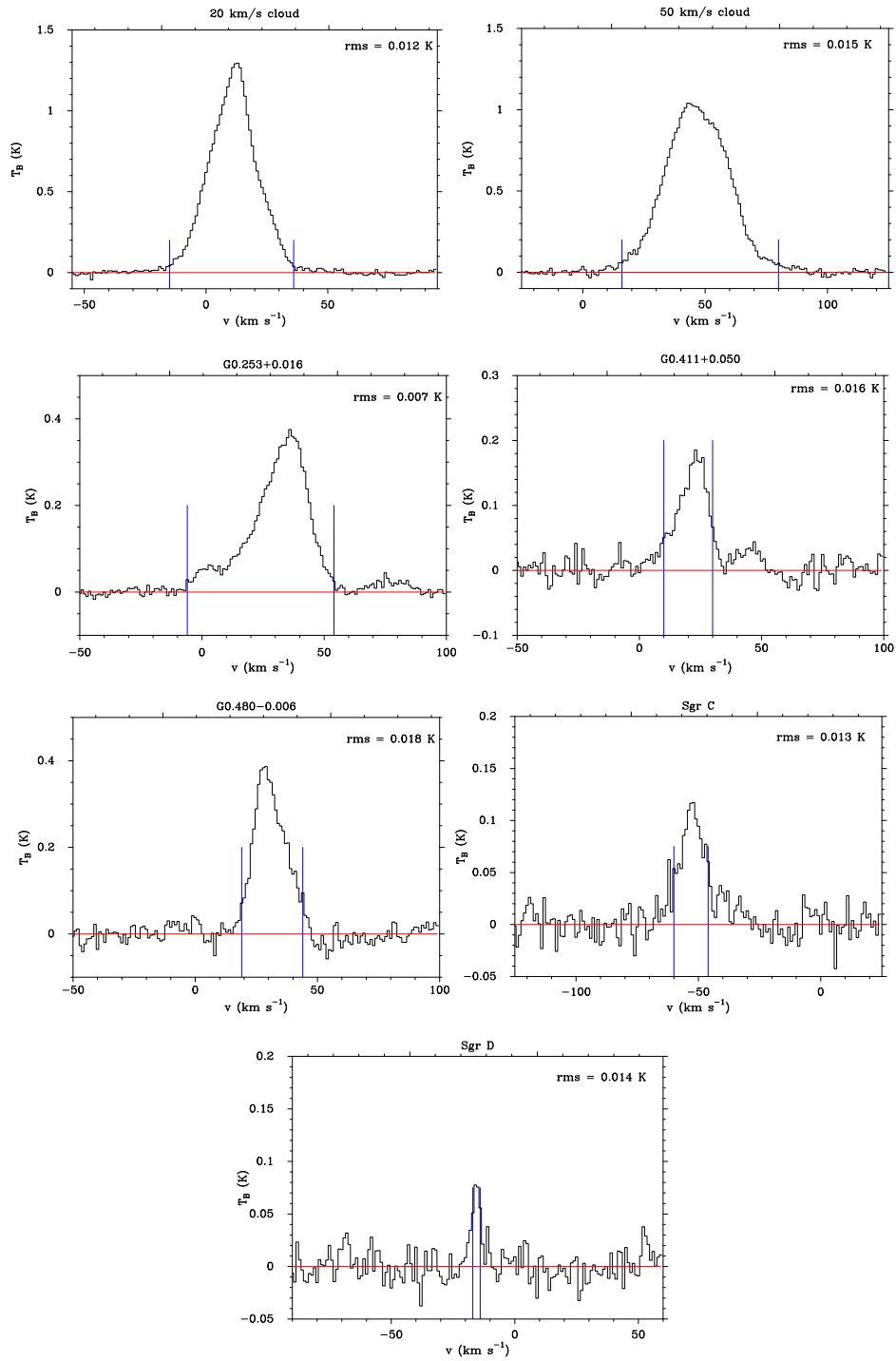
Appendix D: $\text{H}_2\text{CO}(3_{0,3}-2_{0,2})$ spectra

Fig. D.1. $\text{H}_2\text{CO}(3_{0,3}-2_{0,2})$ spectra, averaged over the whole OTF map of each source. The blue lines indicate the velocity range of the whole source where the line emission is above 3σ . The red line shows the fitted baseline (rms value in *upper right corner*).

Appendix E: Integrated intensity maps

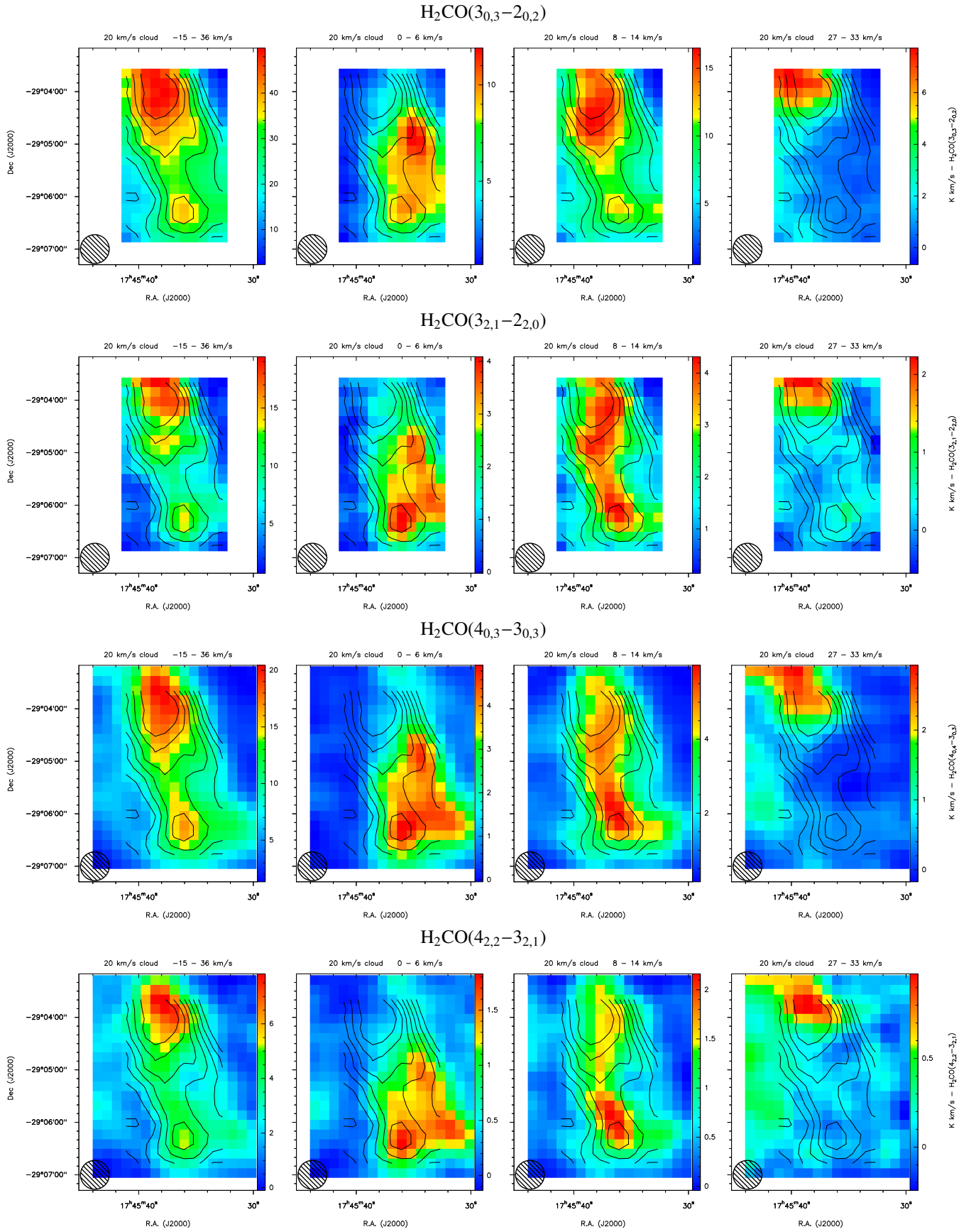


Fig. E.1. Integrated intensities of the para-H₂CO lines at 218 and 291 GHz in the 20 km s⁻¹ cloud. The contours show the moment 0 map of the $\text{H}_2\text{CO}(3_{0,3}-2_{0,2})$ transition, produced over the whole velocity range of the source (levels: 30–90% of the maximum in steps of 10%). The circle in the lower left corner shows the 33'' beam.

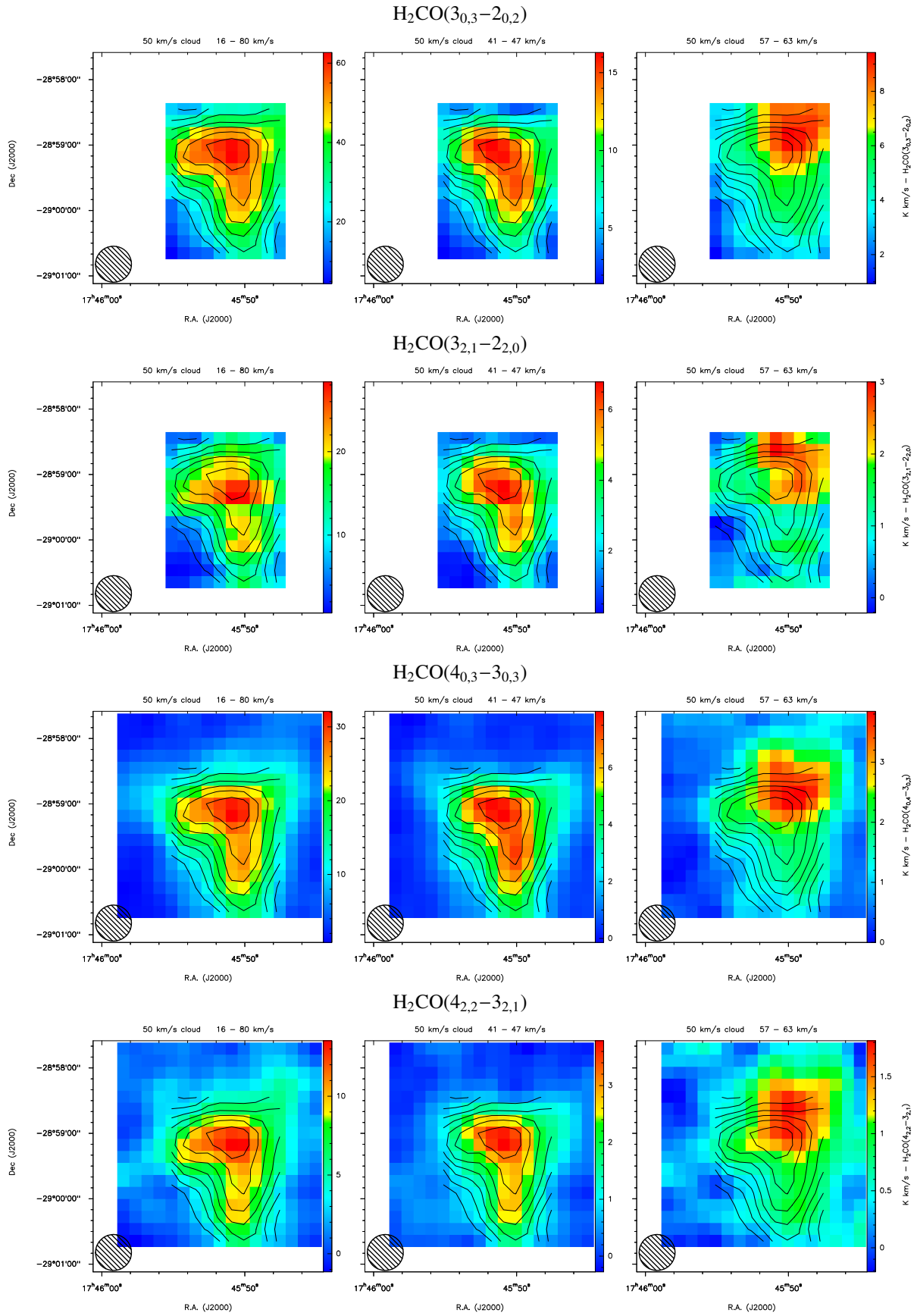


Fig. E.2. As Fig. E.1 for the 50 km s⁻¹ cloud.

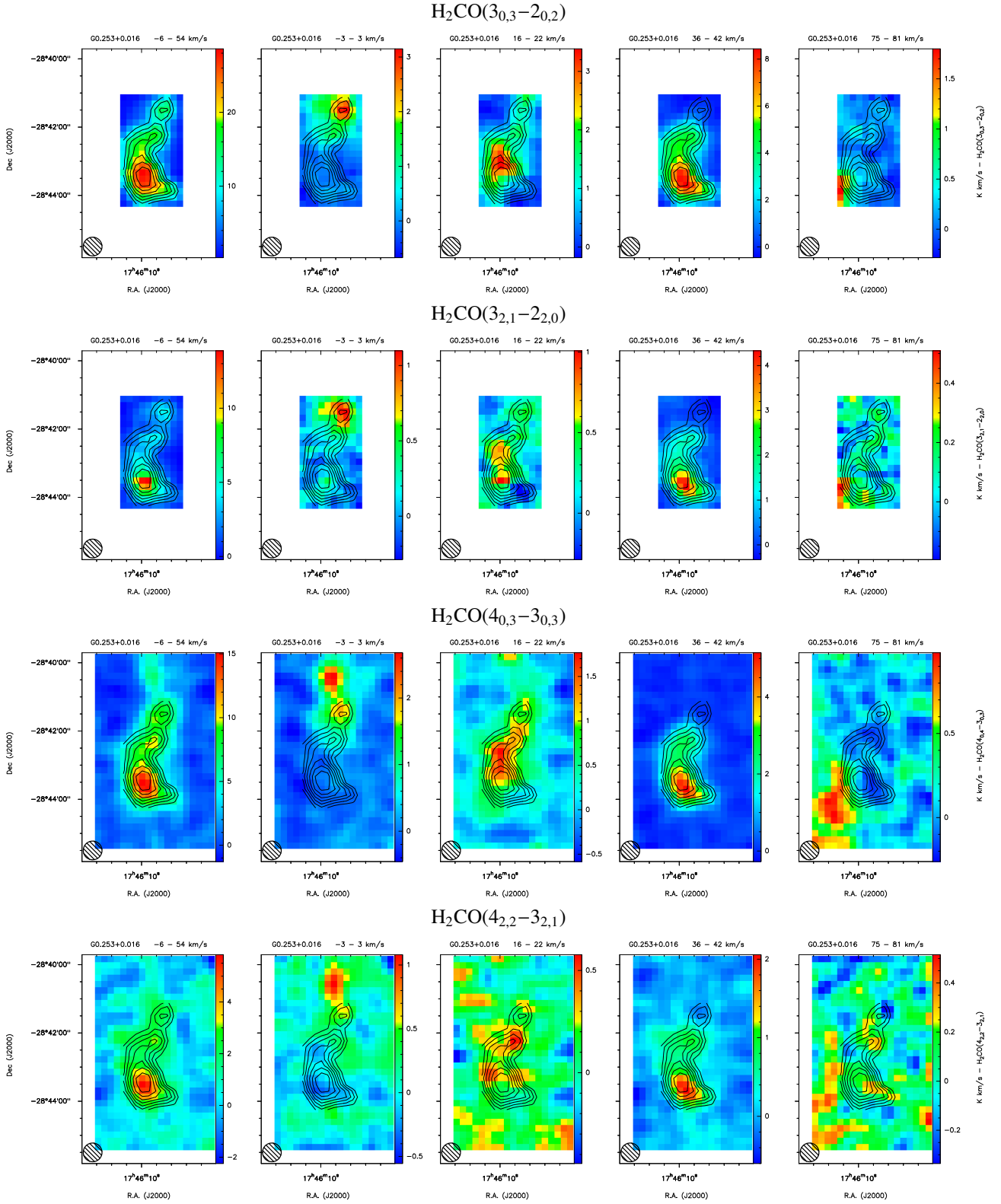


Fig. E.3. As Fig. E.1 for G0.253+0.016.

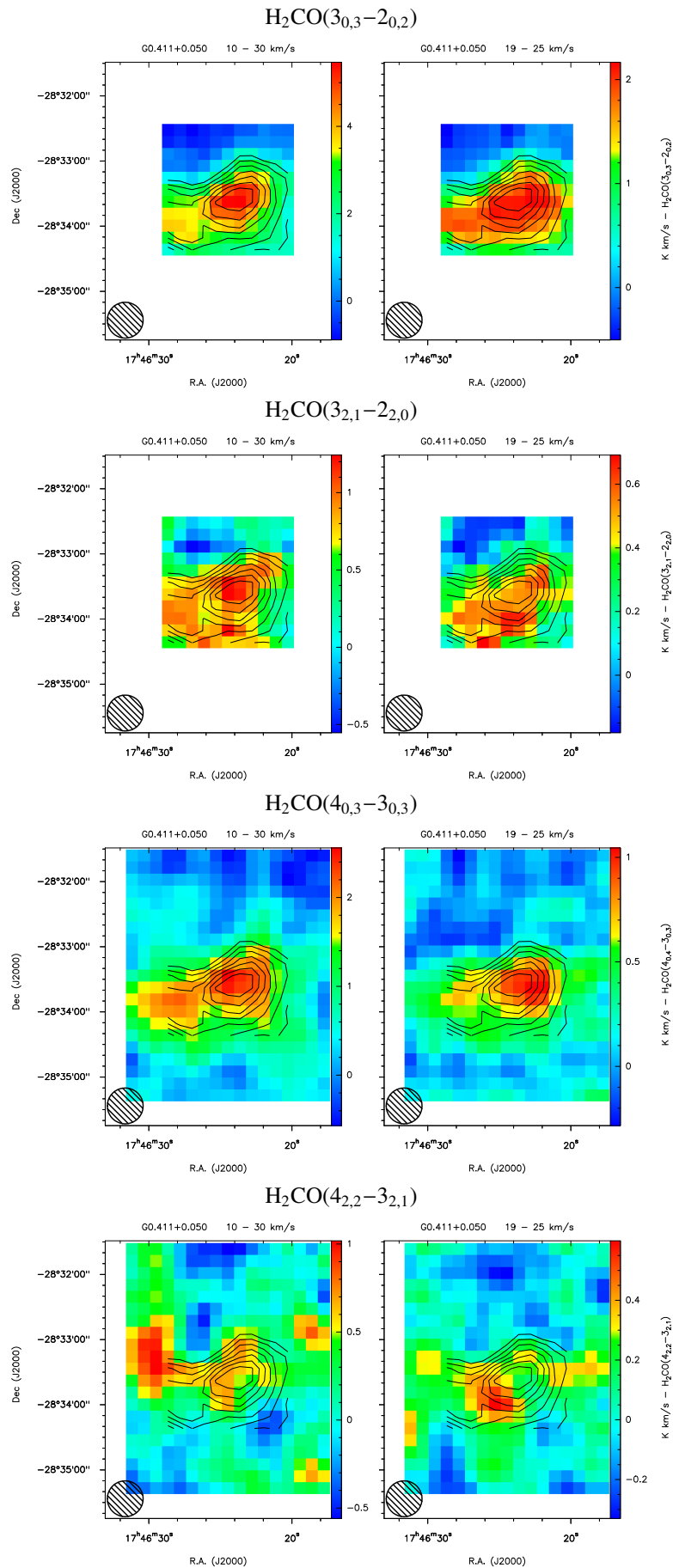


Fig. E.4. As Fig. E.1 for G0.411+0.050.

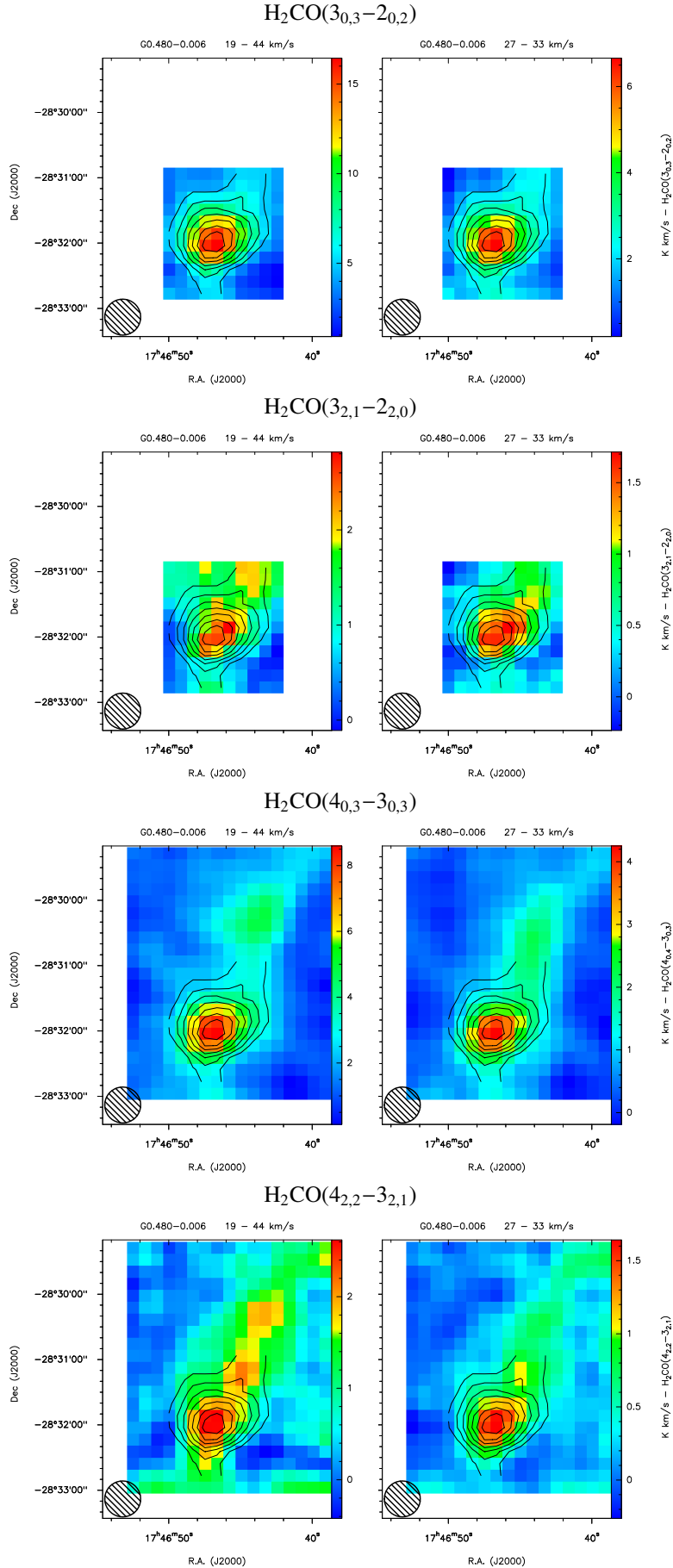


Fig. E.5. As Fig. E.1 for G0.480-0.006.

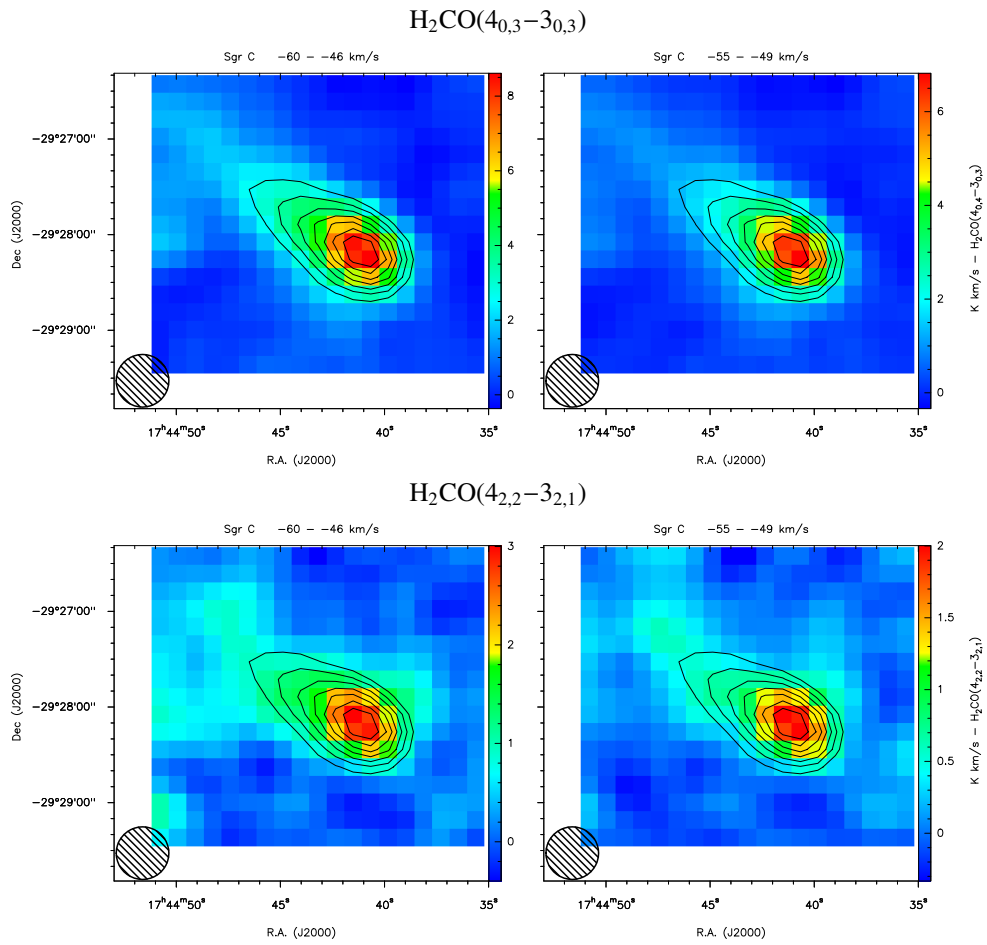


Fig. E.6. As Fig. E.1 for Sgr C.

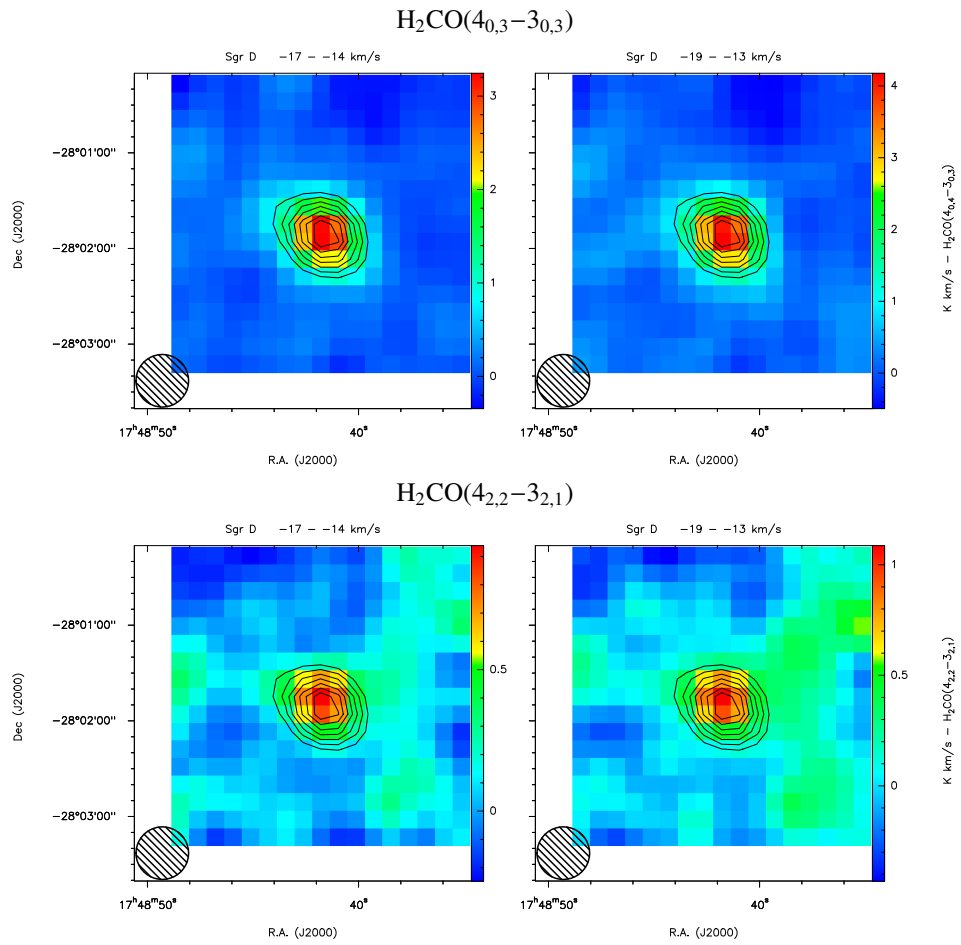


Fig. E.7. As Fig. E.1 for Sgr D.

Appendix F: Integrated intensity ratio and uncertainty maps

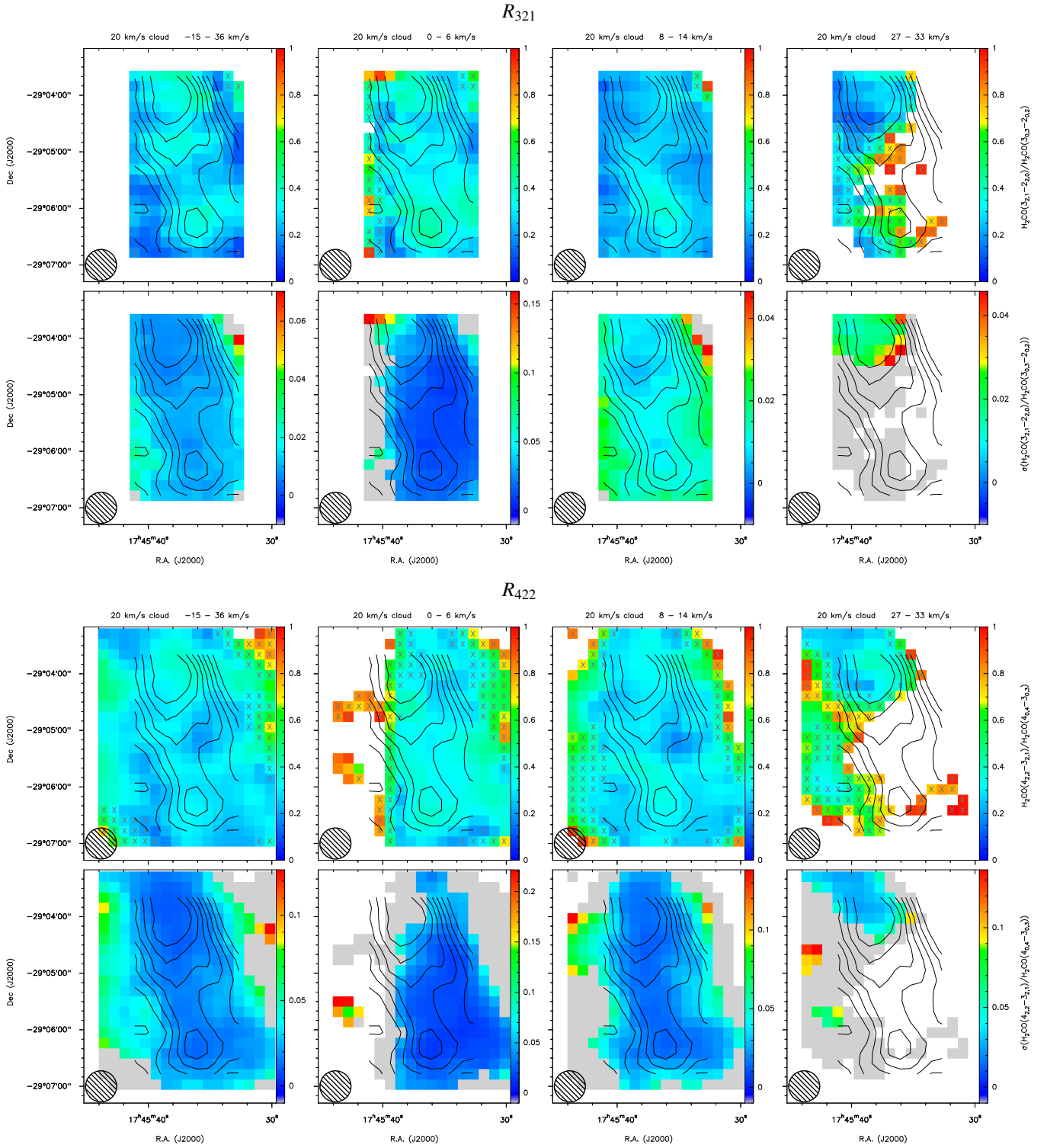


Fig. F.1. Integrated intensity ratio (*upper panels*) and uncertainty (*lower panels*) maps of the 20 km s^{-1} cloud (contours as in Fig. E.1). Upper limits of the ratios are indicated with Xs. The corresponding pixels in the uncertainty maps are shown in gray. The circle in the lower left corner shows the $33''$ beam.

R_{404}

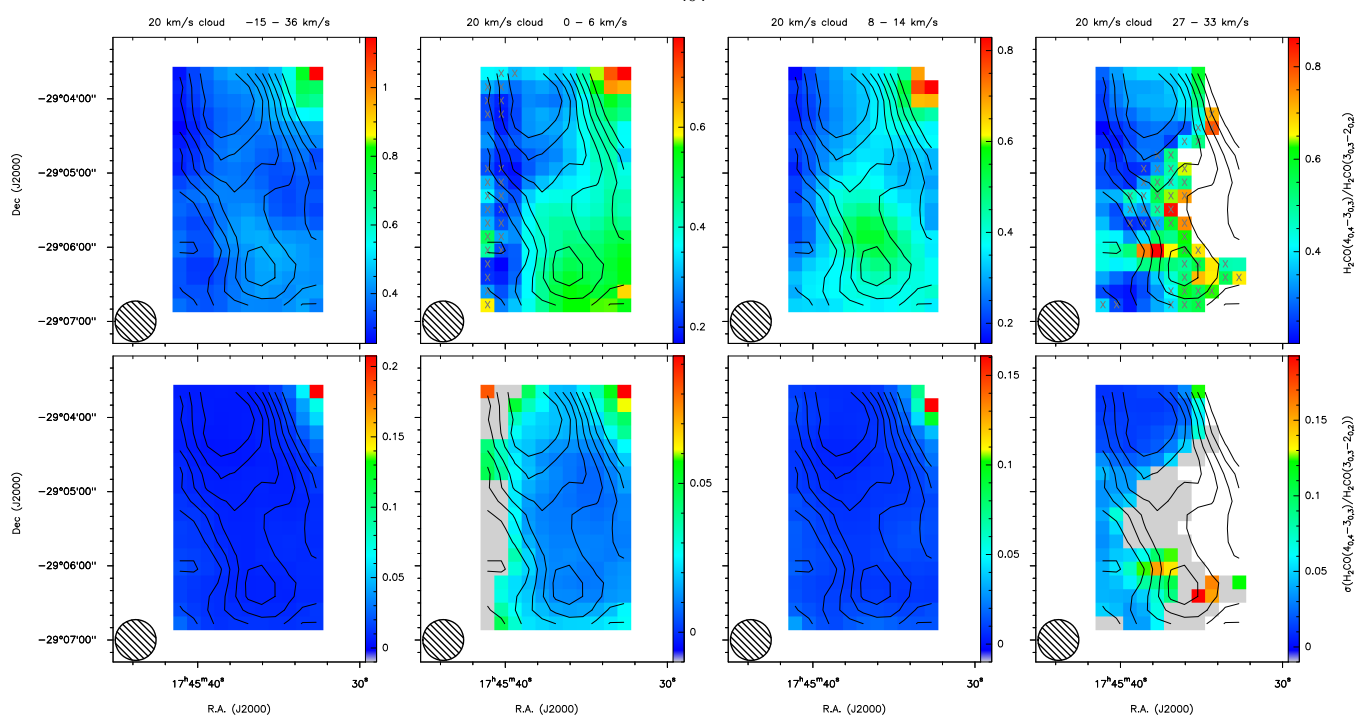


Fig. F.1. continued.

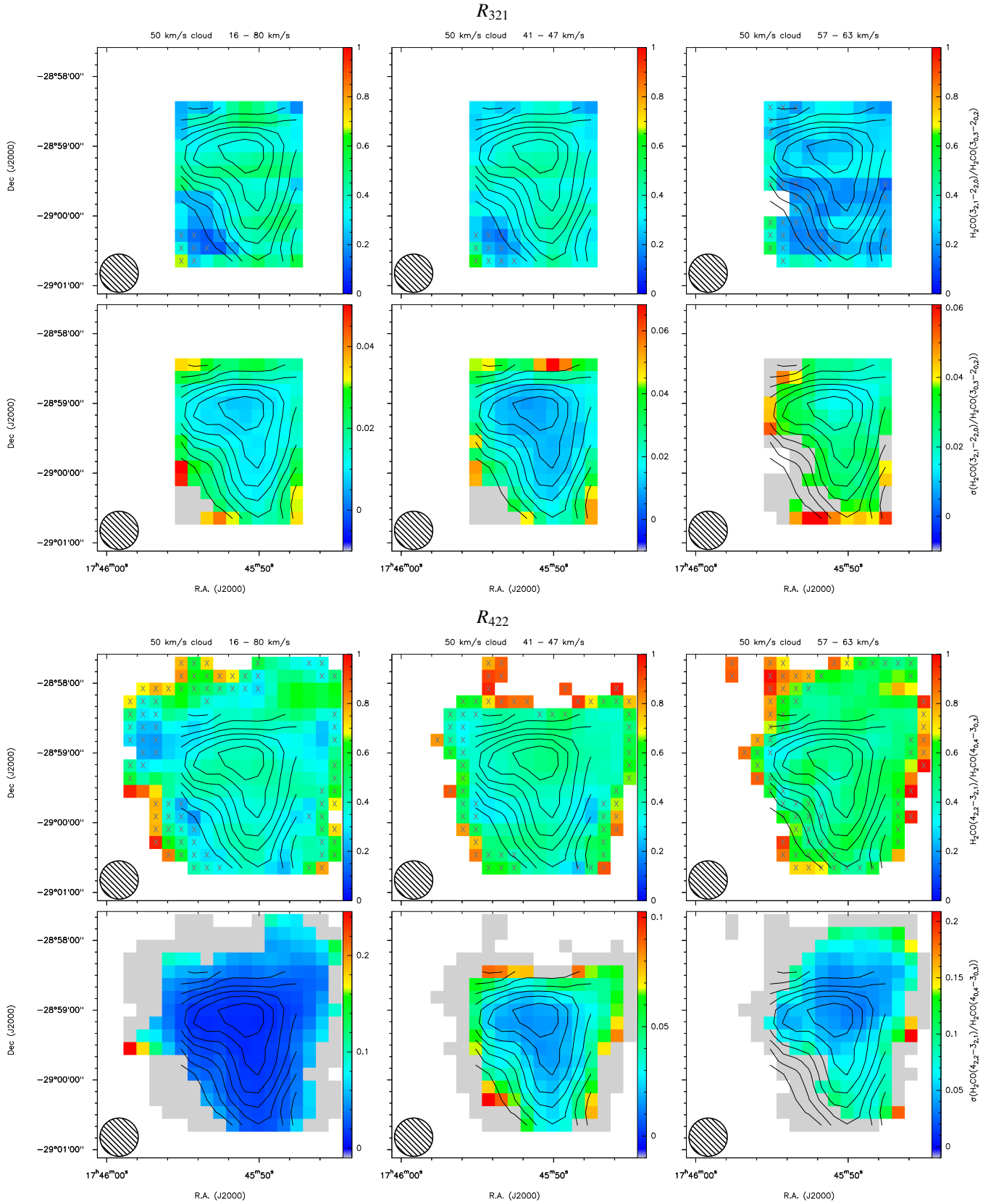


Fig. F.2. As Fig. F.1 for the 50 km s⁻¹ cloud.

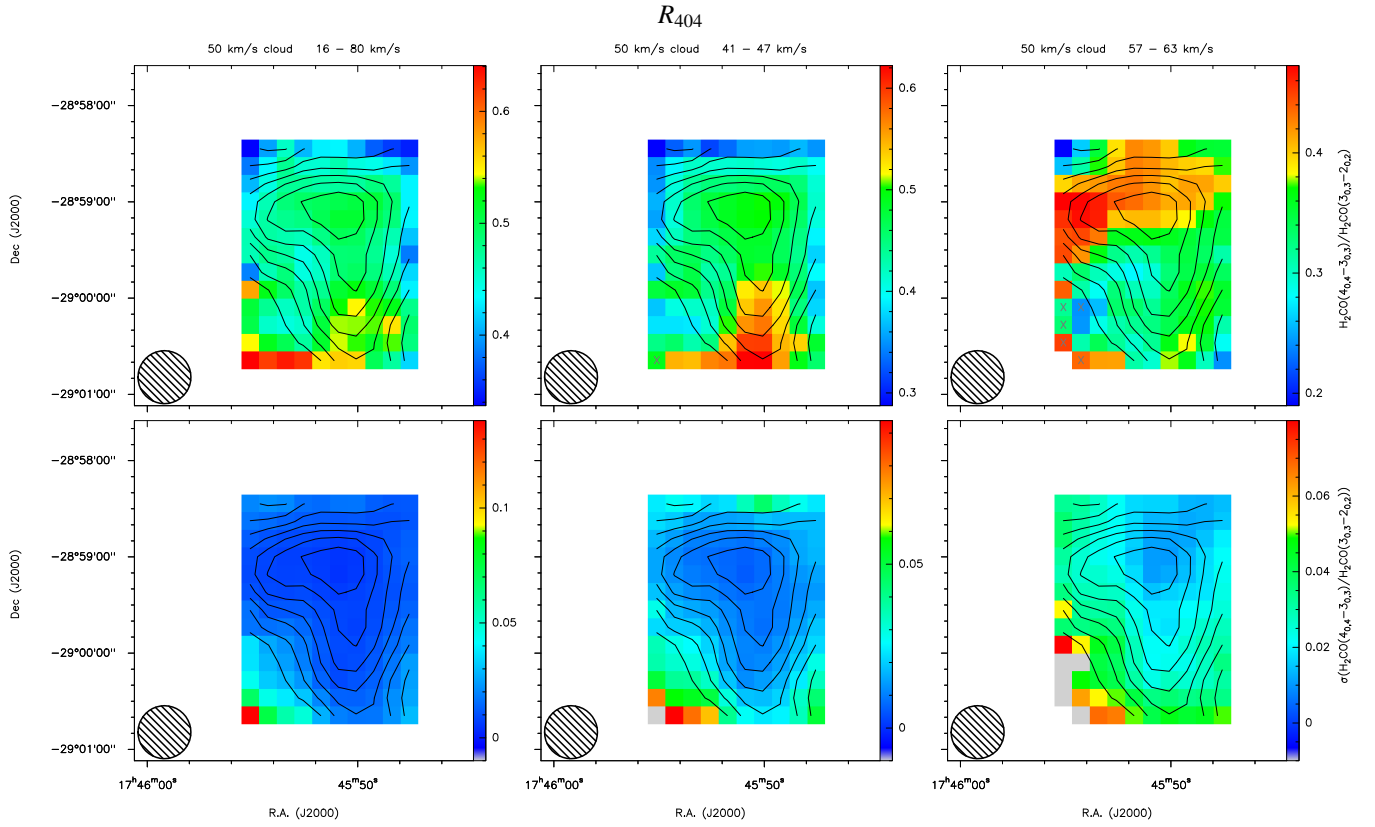


Fig. F.2. continued.

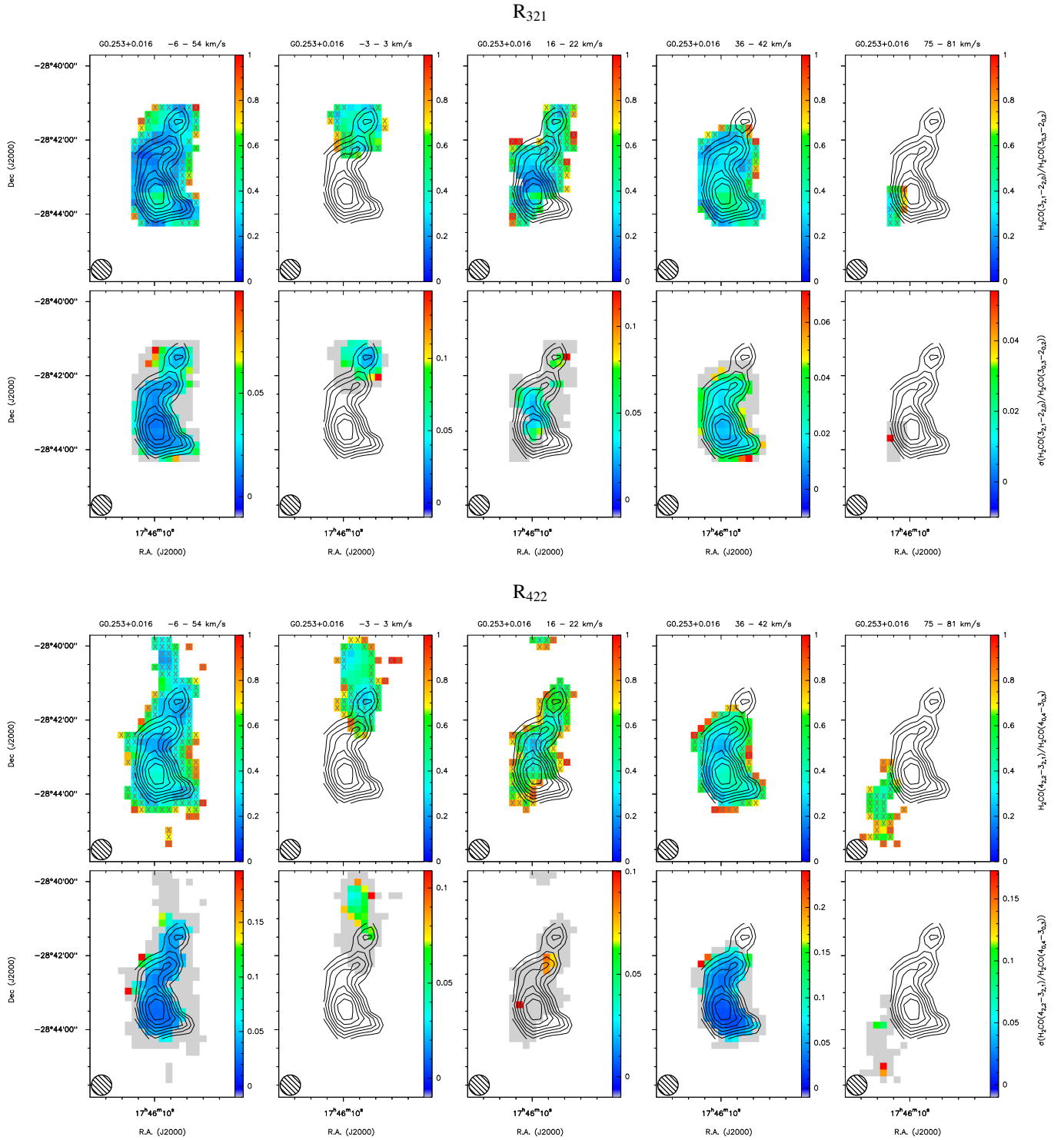


Fig. F.3. As Fig. F.1 for G0.253+0.016.

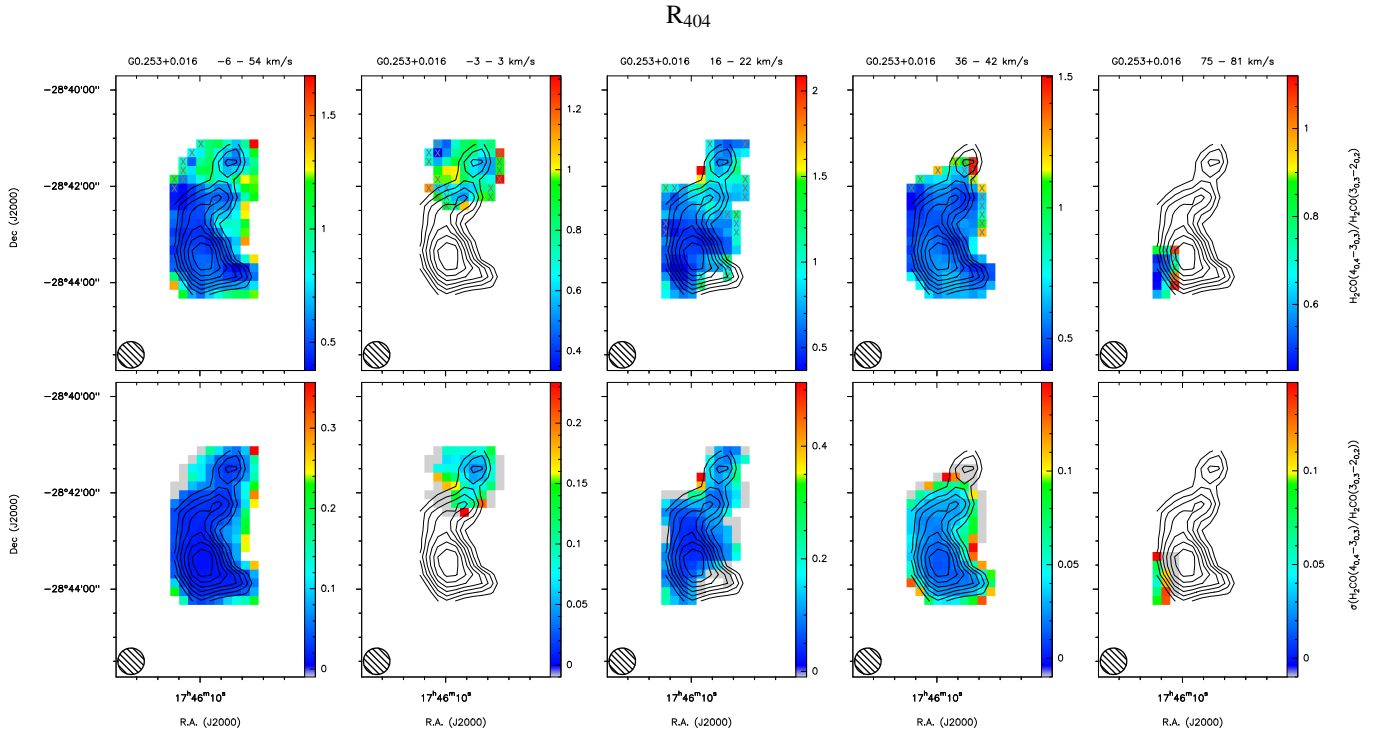


Fig. F.3. continued.

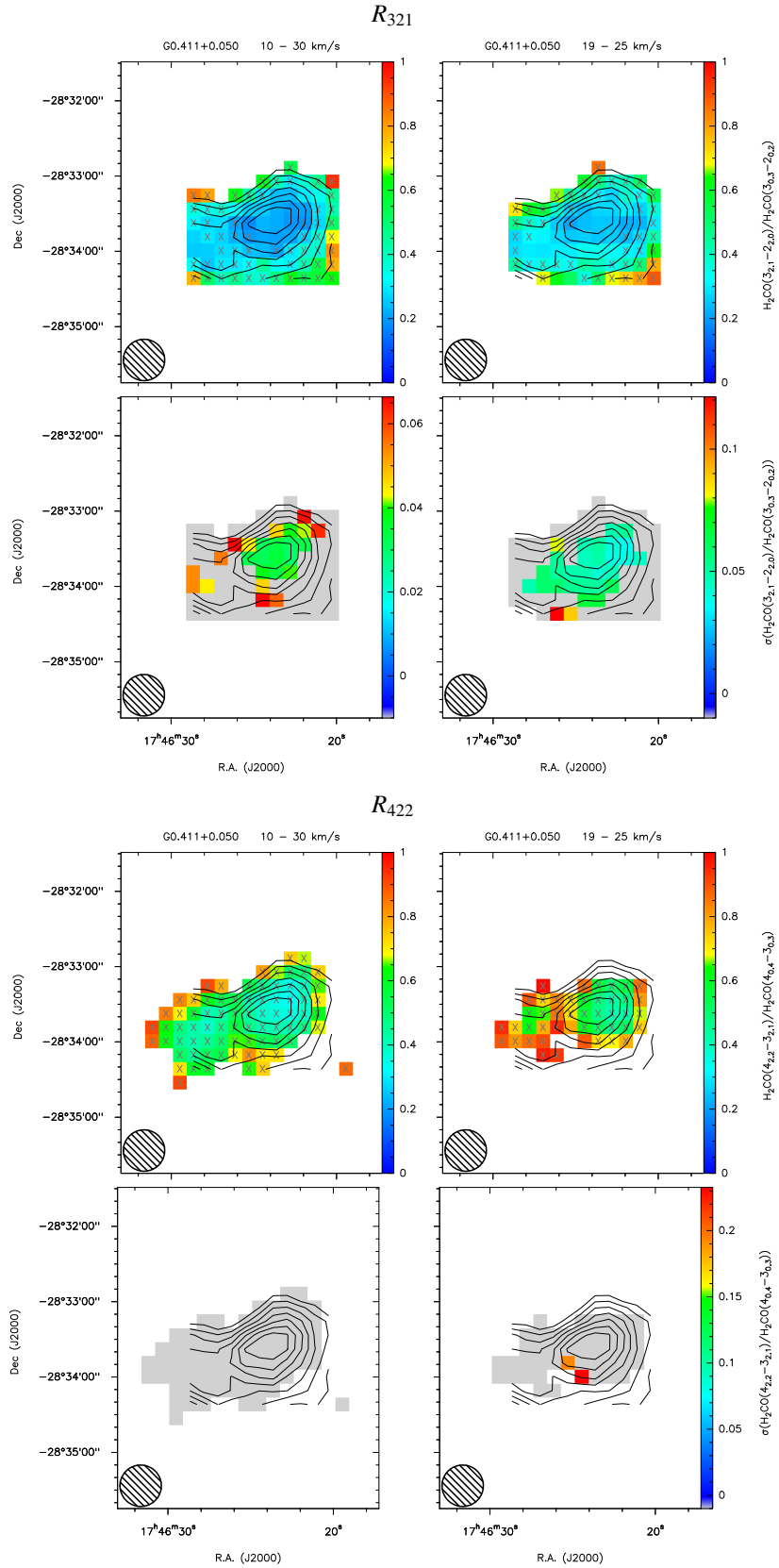


Fig. F.4. As Fig. F.1 for G0.411+0.050.

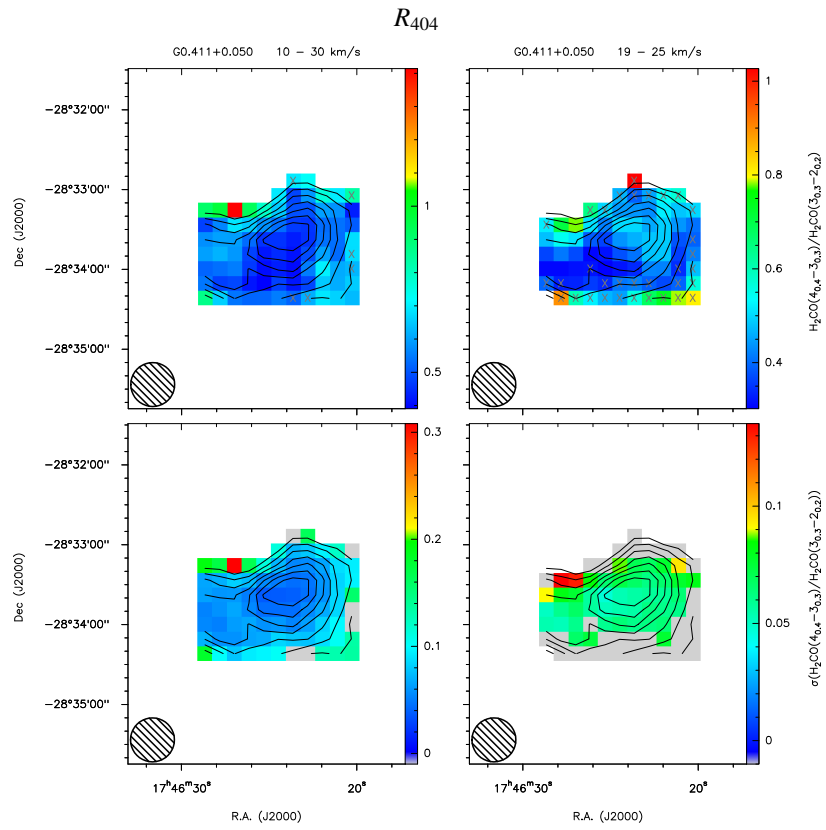


Fig. F.4. continued.

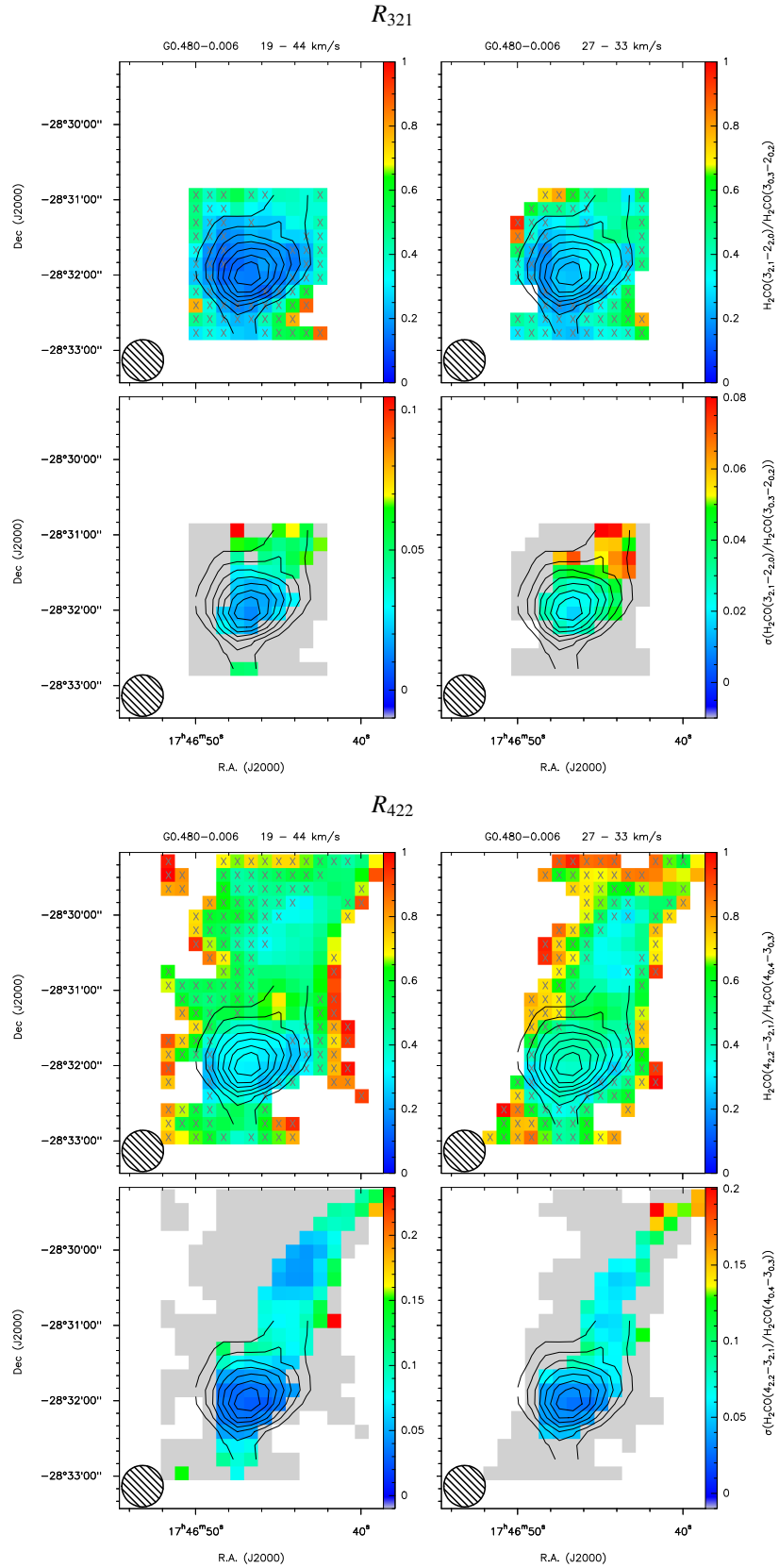


Fig. F.5. As Fig. F.1 for G0.480-0.006.

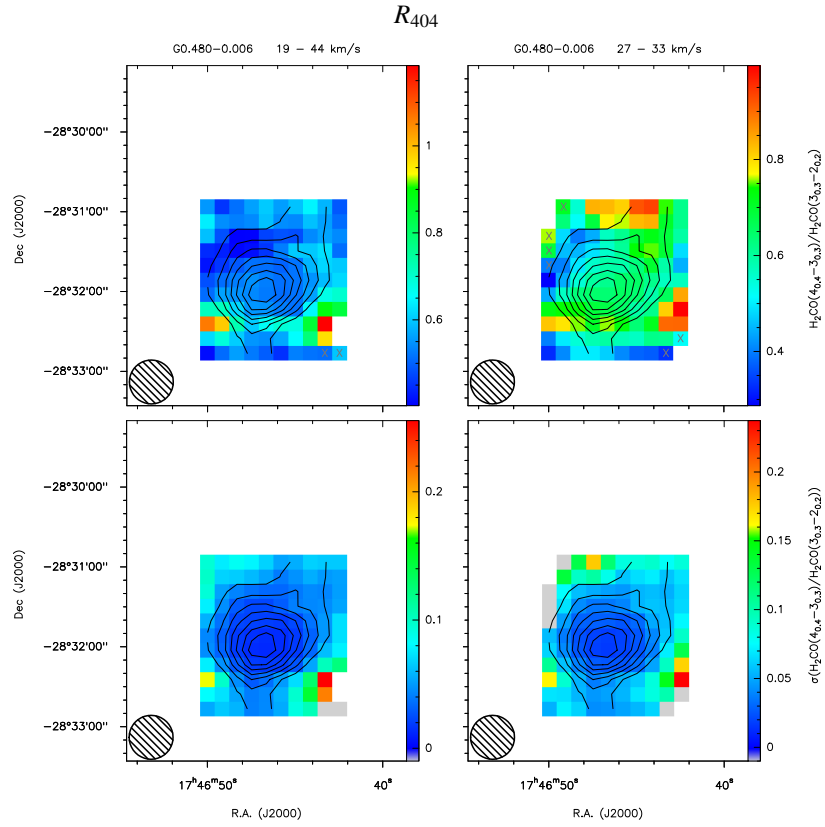


Fig. F.5. continued.

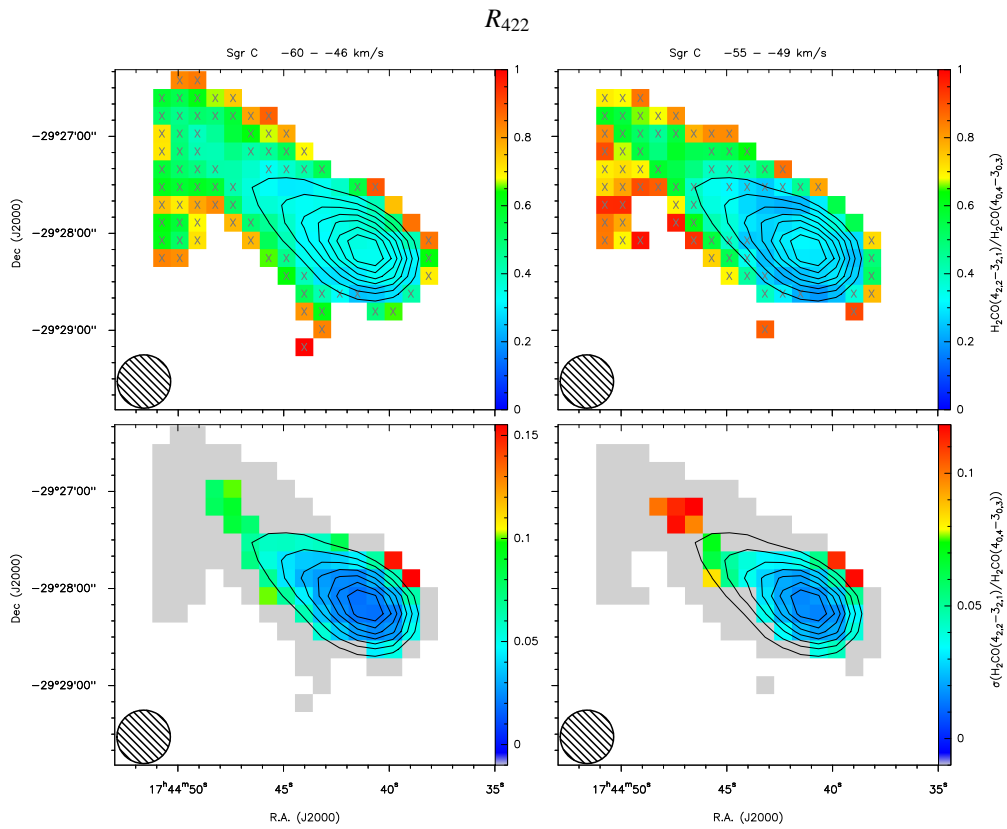


Fig. F.6. As Fig. F.1 for Sgr C.

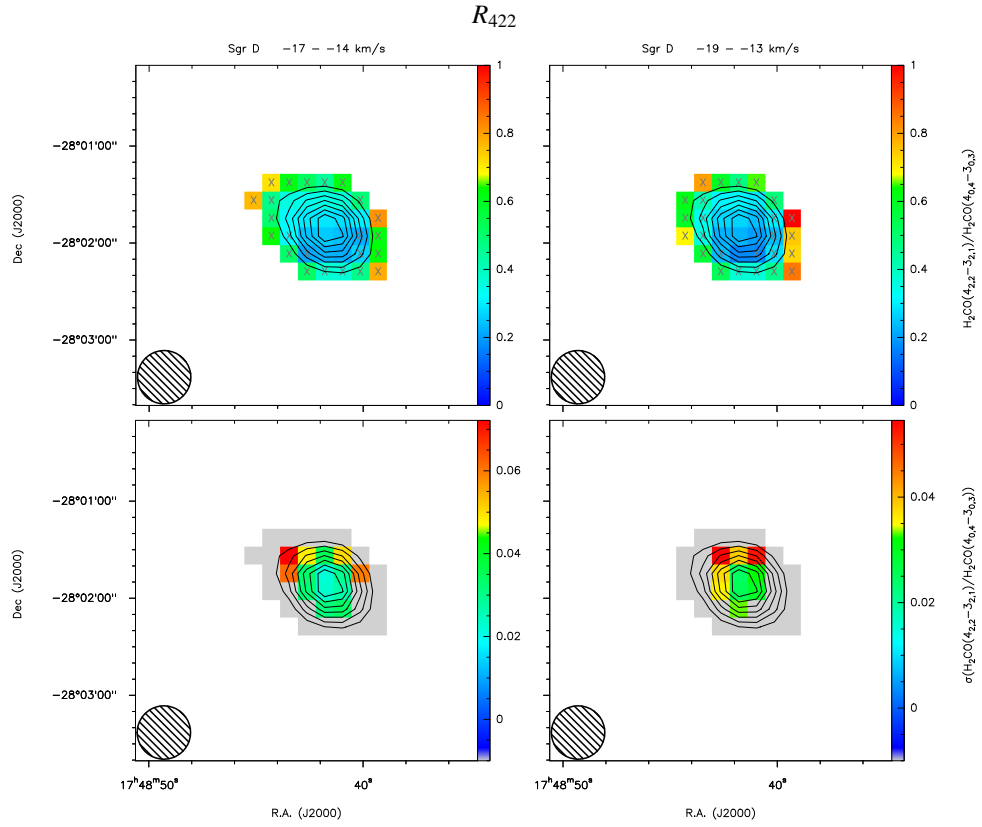


Fig. F.7. As Fig. F.1 for Sgr D.

Appendix G: Modeling

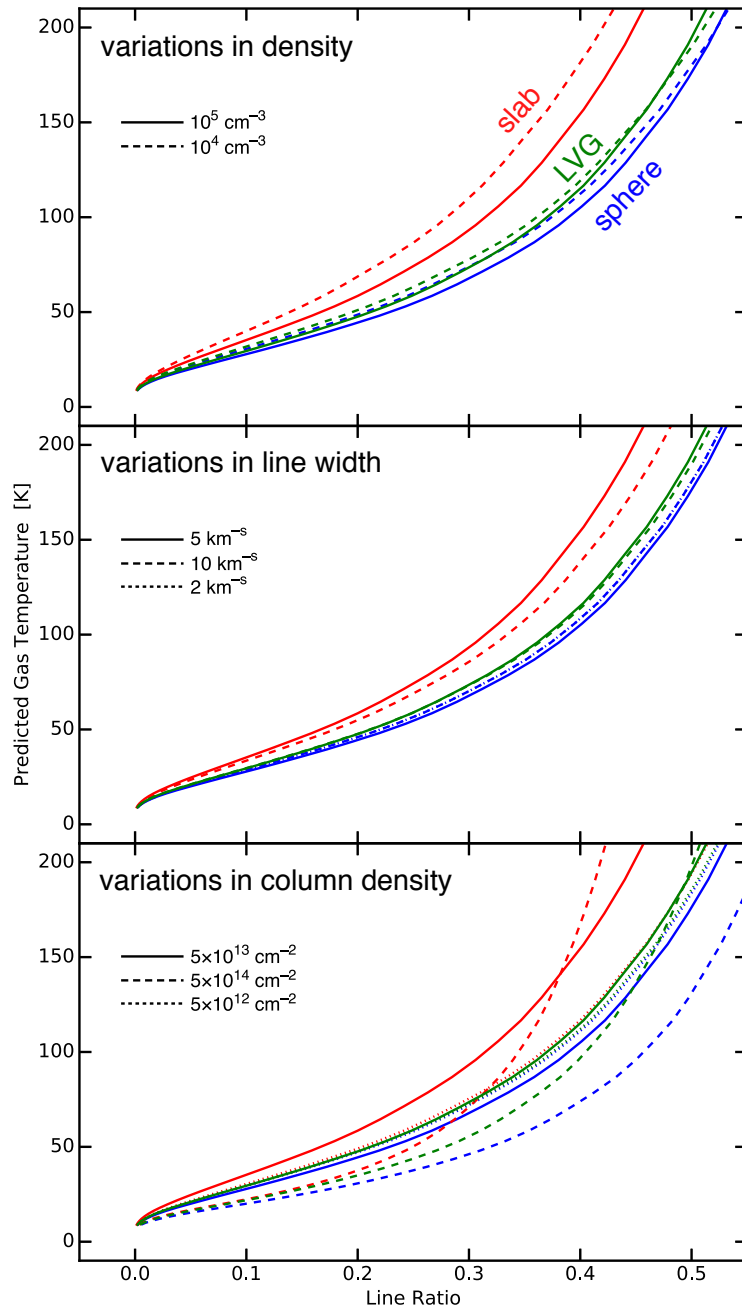


Fig. G.1. Impact of different assumptions in column density, density, line width, and geometry on the estimated temperatures. The solid blue line is always the fiducial case used to obtain the temperatures presented in this paper.

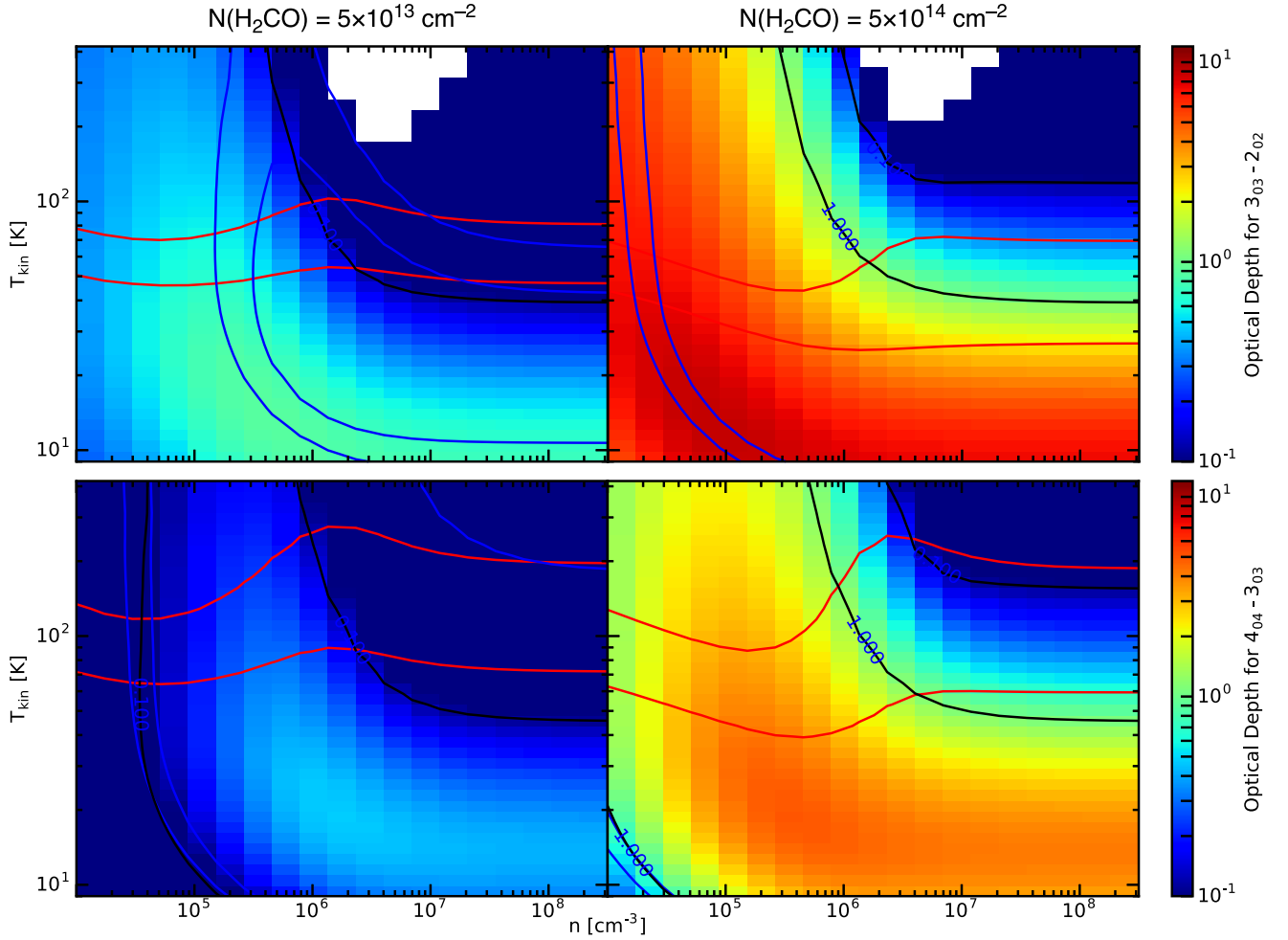
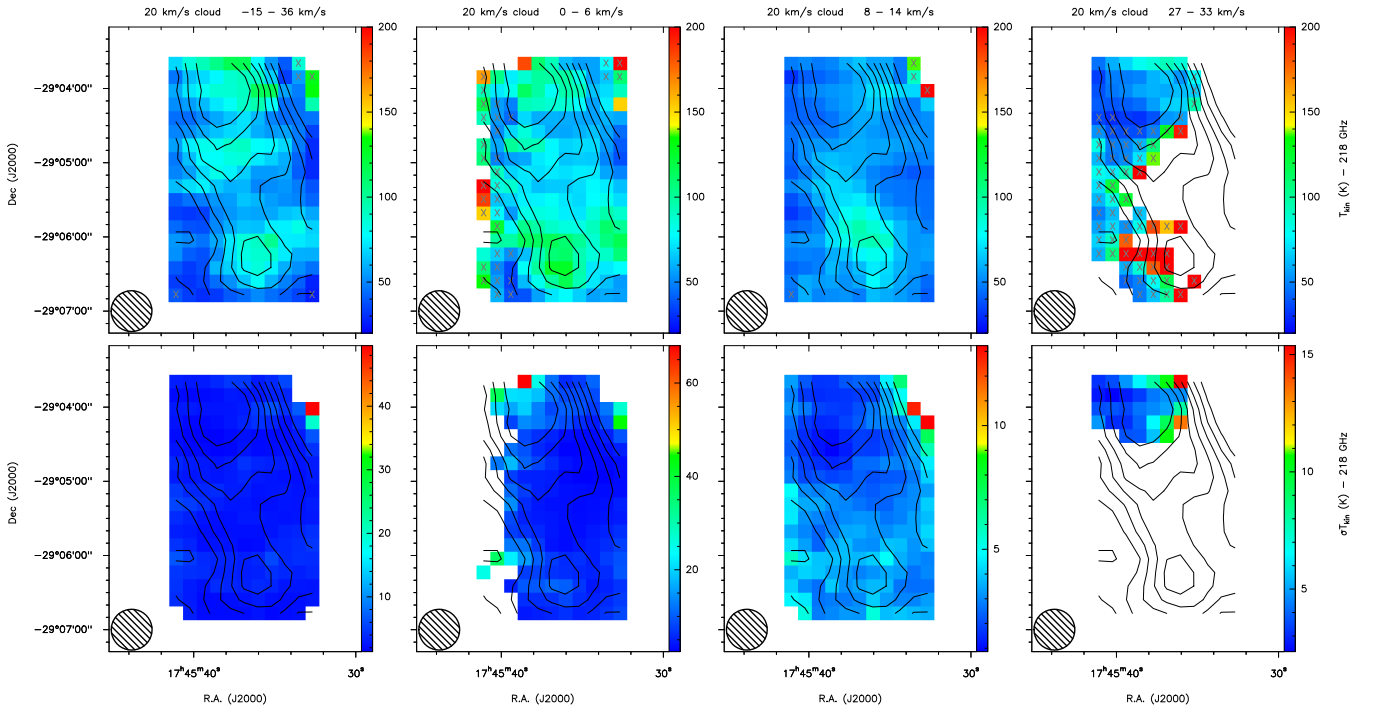


Fig. G.2. Impact of line optical depth. The optical depths shown on the left are calculated for the fiducial case (see Sect. 4.2), while those on the right are for an increased column density of $5 \times 10^{14} \text{ cm}^{-2}$. The red lines indicate the observed line ratios of 0.25 (*top panel*) and 0.35 (*bottom panel*) at 218 and 291 GHz, respectively, in the 8–14 km s^{-1} slice of the 20 km s^{-1} cloud. The blue lines indicate an intensity of 15 K km s^{-1} at 218 GHz (*top panel*) and of 4 K km s^{-1} at 291 GHz (*bottom panel*), respectively, in the same slice. Black lines give optical depth contours. The lines come in pairs since we allow for $\pm 20\%$ variation in drawing. Simultaneous fits to line ratios and intensities are found in locations where the blue and red lines intersect. At 218 GHz (*top panel*) these simultaneous matches require either relatively high densities (*left panel*) or high optical depths (*right panel*).

Appendix H: Temperature maps

218 GHz temperatures



291 GHz temperatures

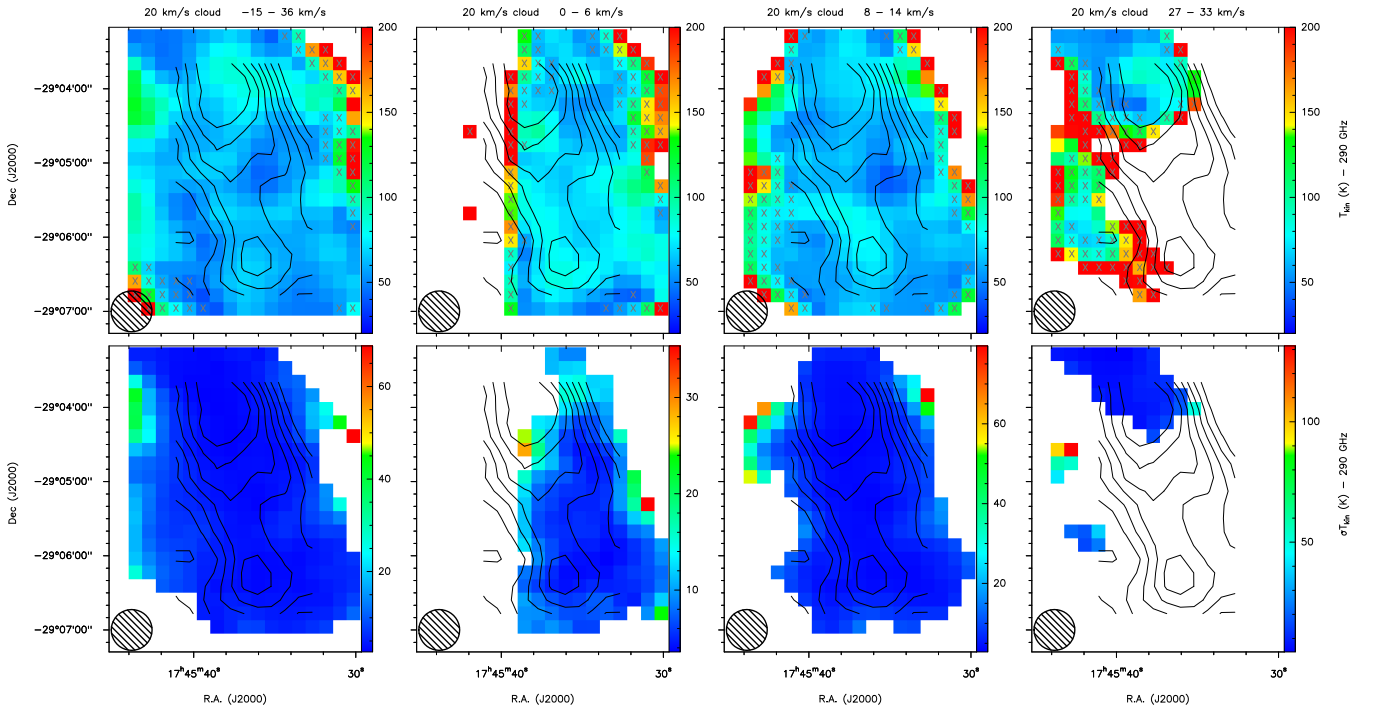
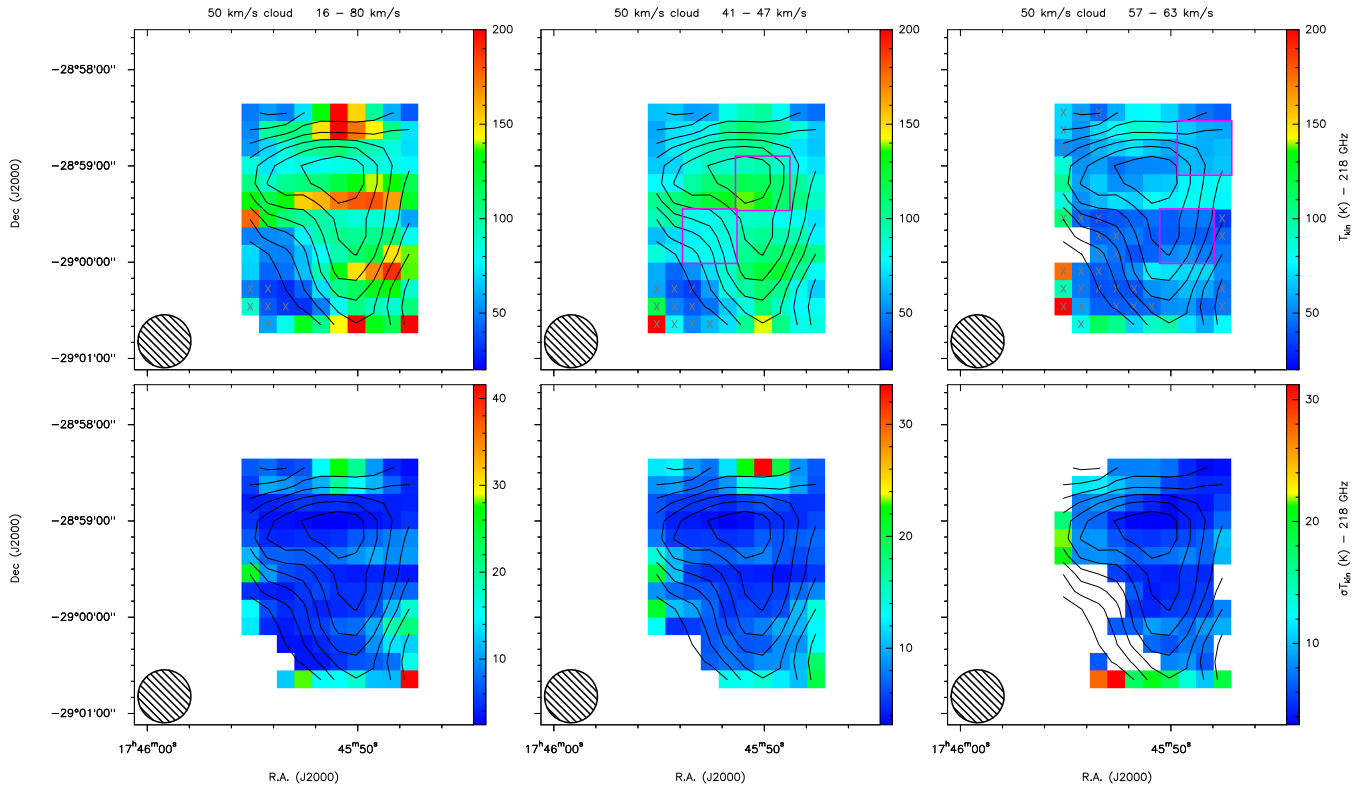


Fig. H.1. Temperature (*upper panels*) and uncertainty (*lower panels*) maps of the 20 km s^{-1} cloud (contours as in Fig. E.1). Upper limits of the temperatures are marked with Xs. The corresponding pixels in the uncertainty maps are blanked. The purple squares present the areas over which the emission of the main H_2CO line was integrated to determine the line width, as well as the average temperature (see Sect. 5.3). The circle in the *lower left corner* shows the $33''$ beam.

218 GHz temperatures



291 GHz temperatures

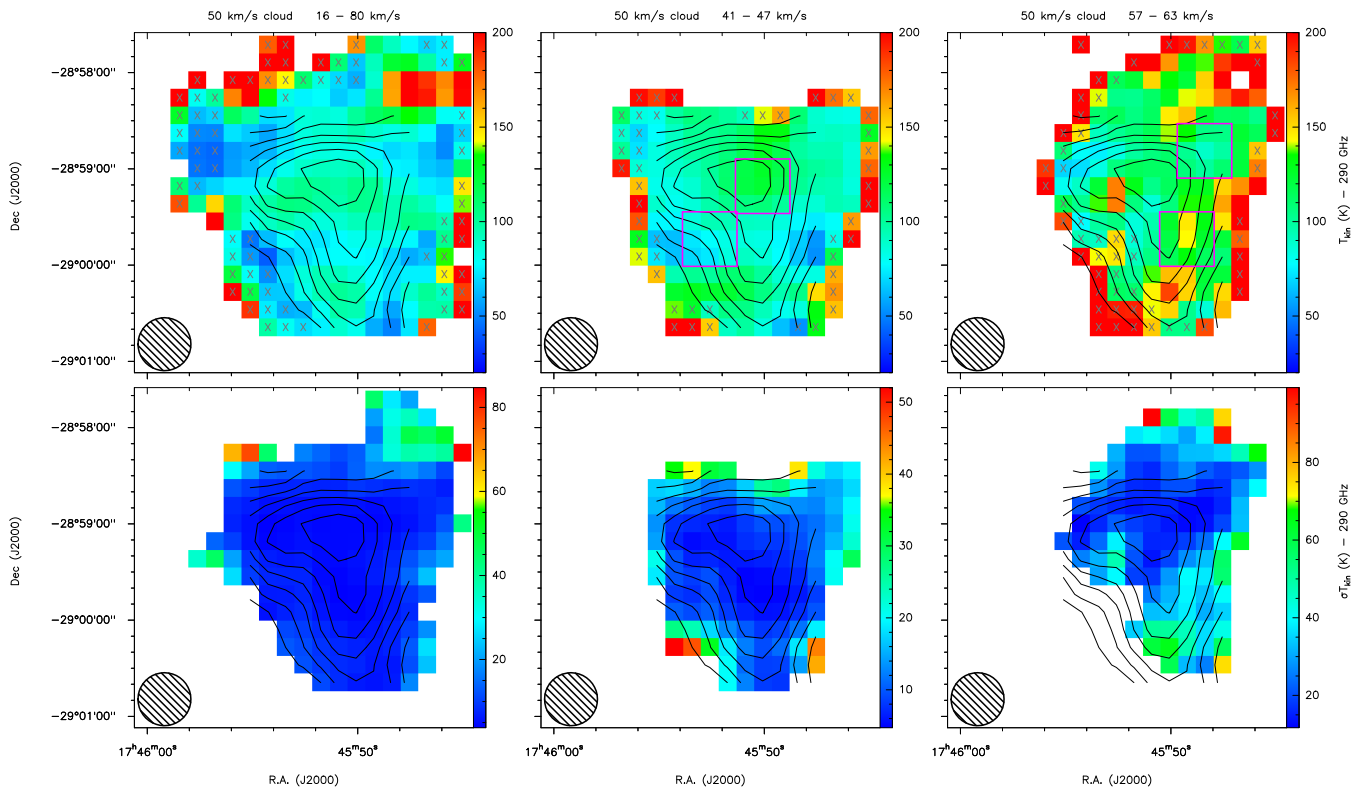
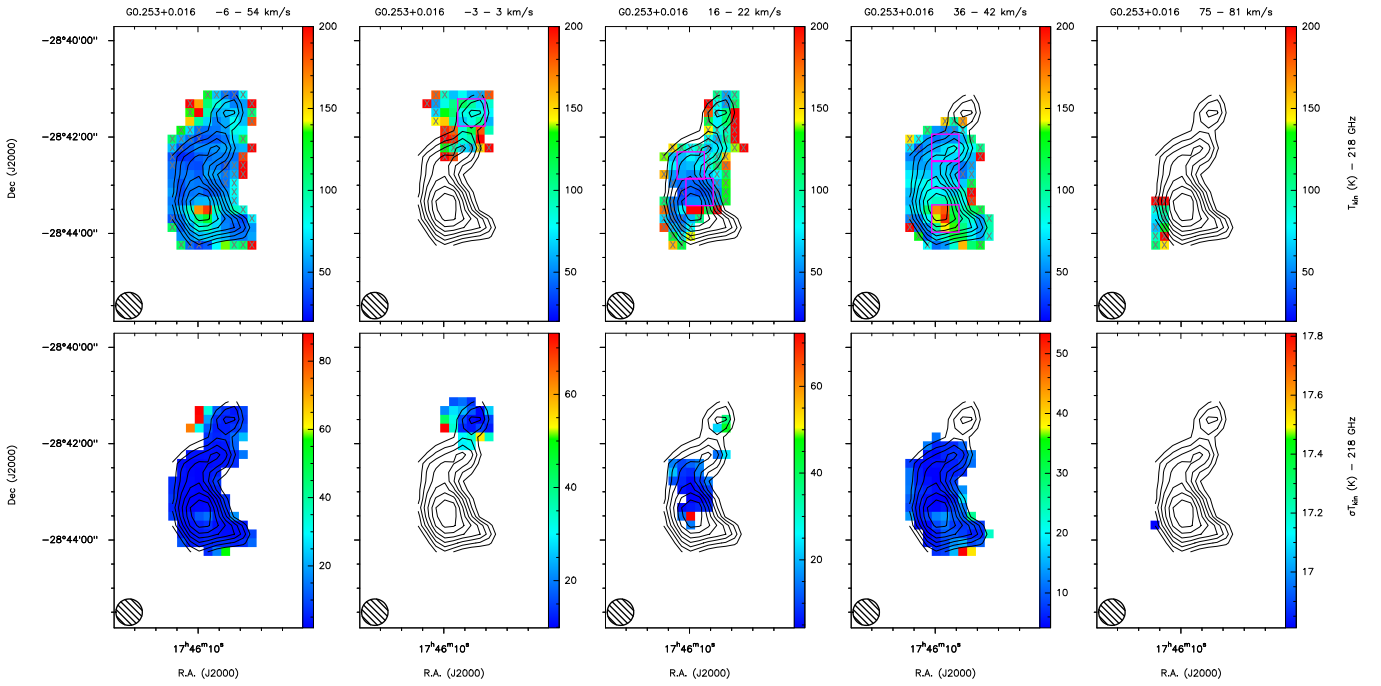


Fig. H.2. As Fig. H.1, for the 50 km s⁻¹ cloud.

218 GHz temperatures



291 GHz temperatures

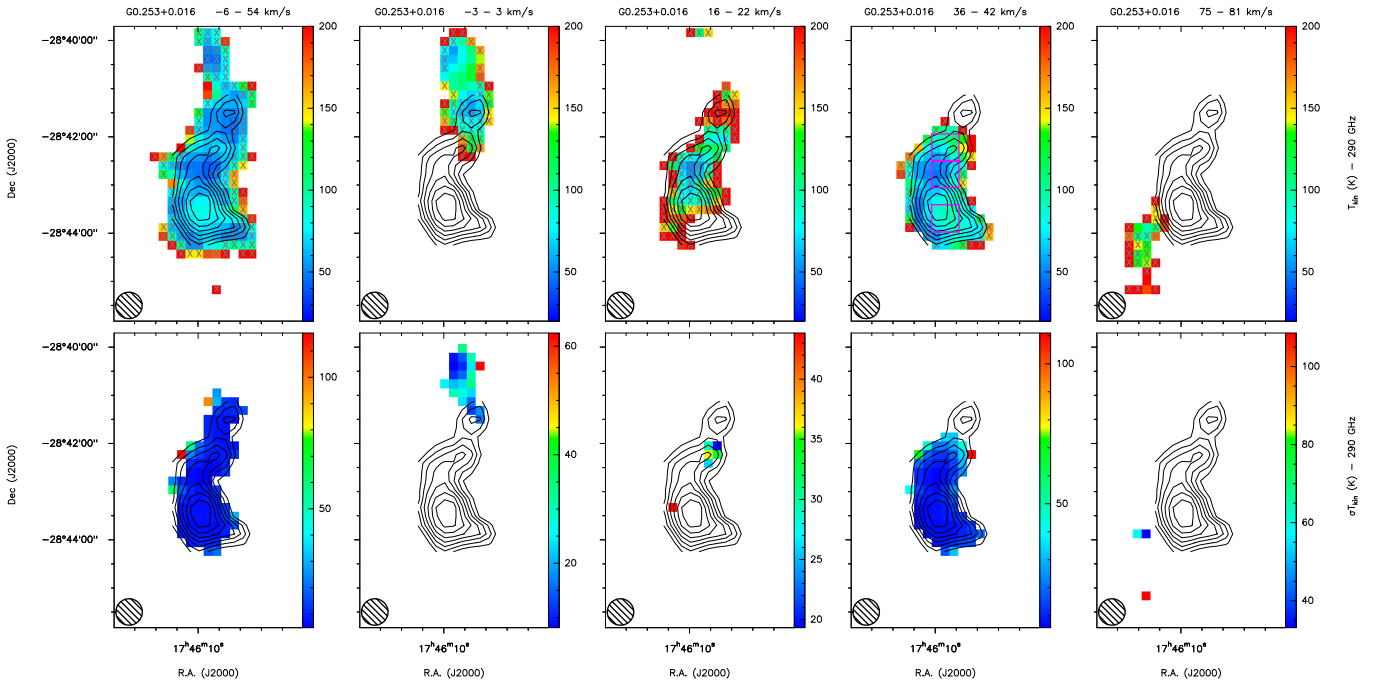
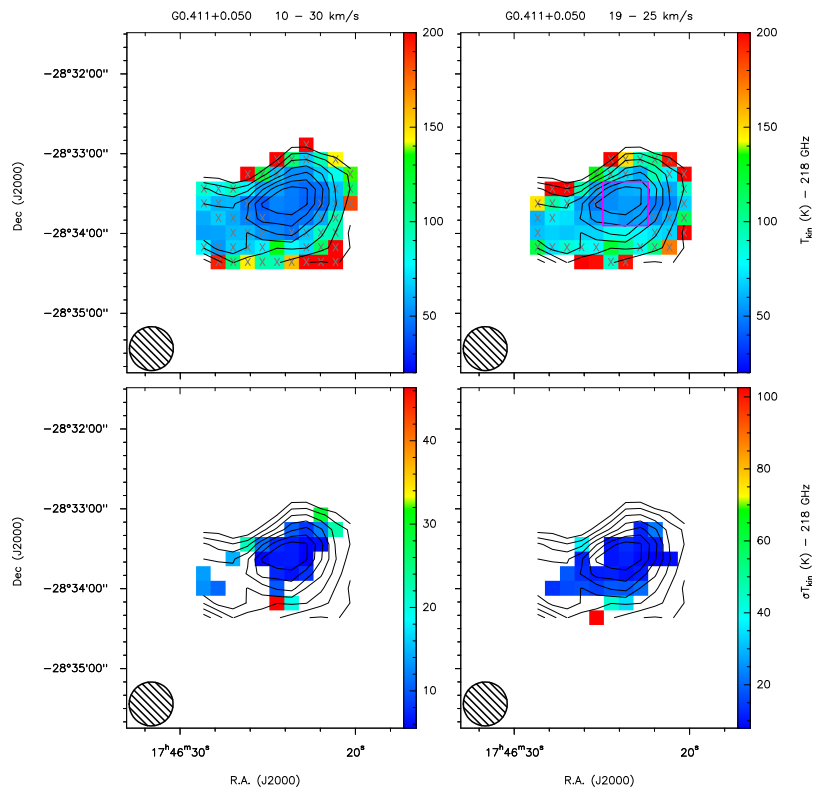


Fig. H.3. As Fig. H.1, for G0.253+0.016.

218 GHz temperatures



291 GHz temperatures

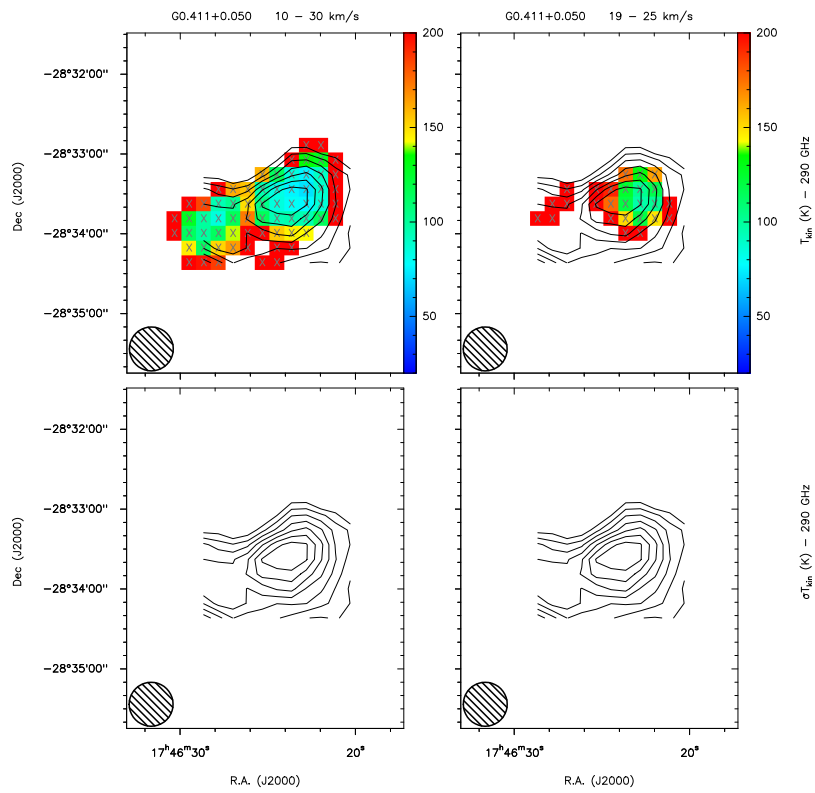


Fig. H.4. As Fig. H.1, for G0.411+0.050.

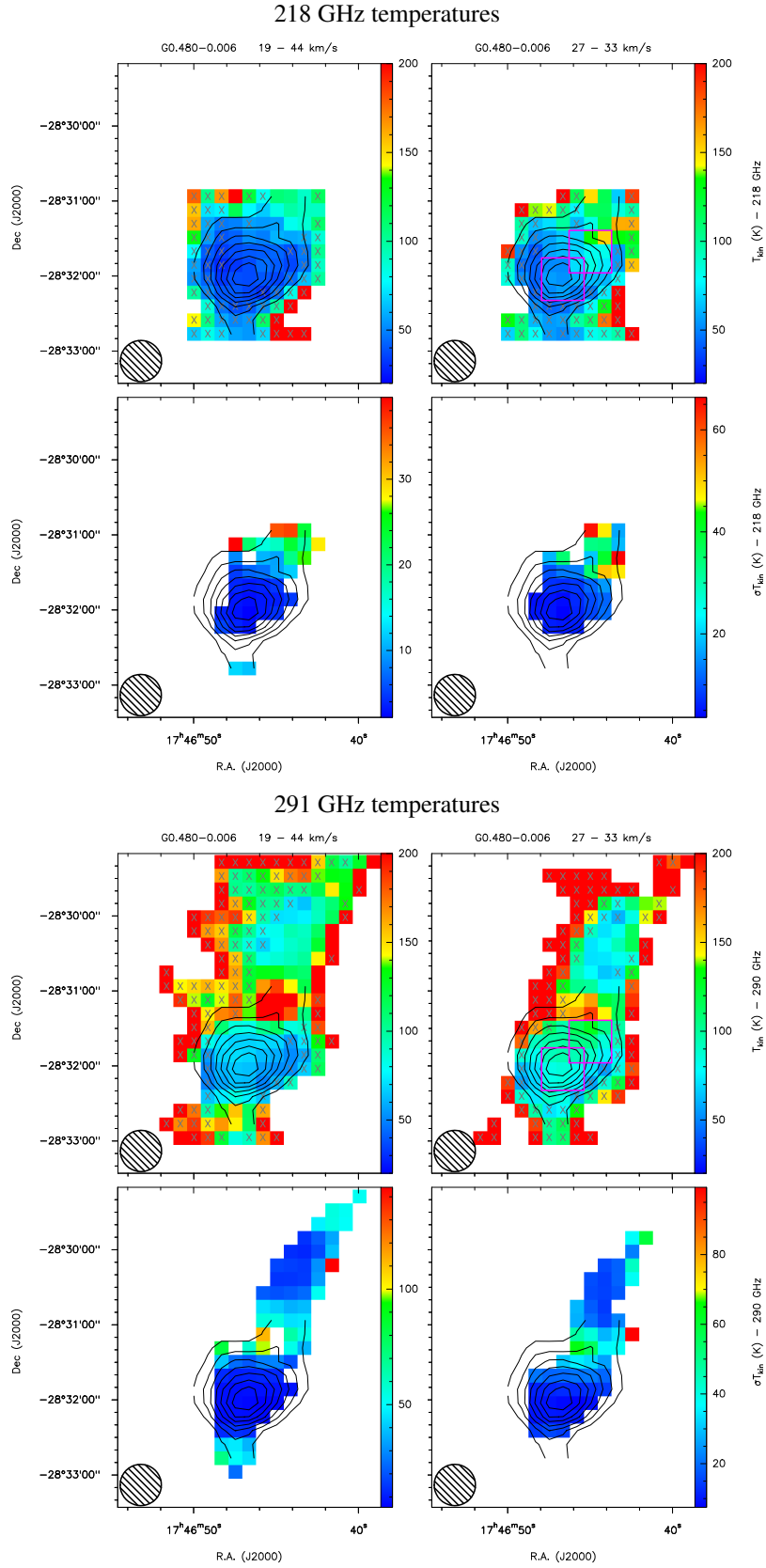


Fig. H.5. As Fig. H.1, for G0.480–0.006.

291 GHz temperatures

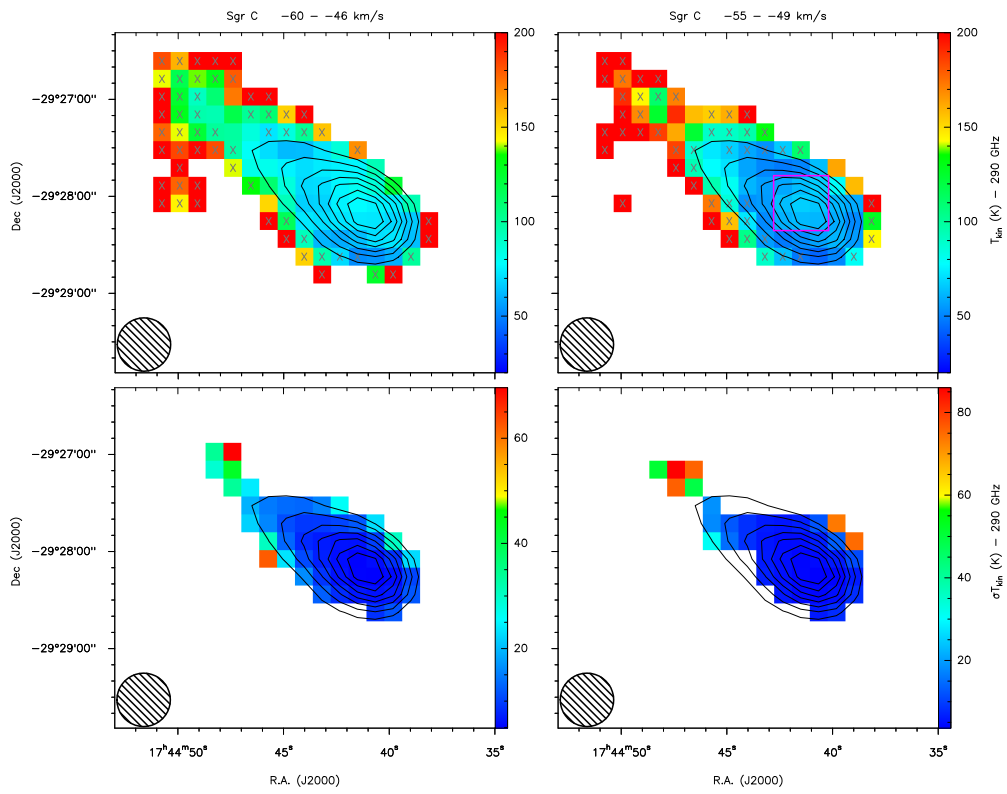


Fig. H.6. As Fig. H.1, for Sgr C.

291 GHz temperatures

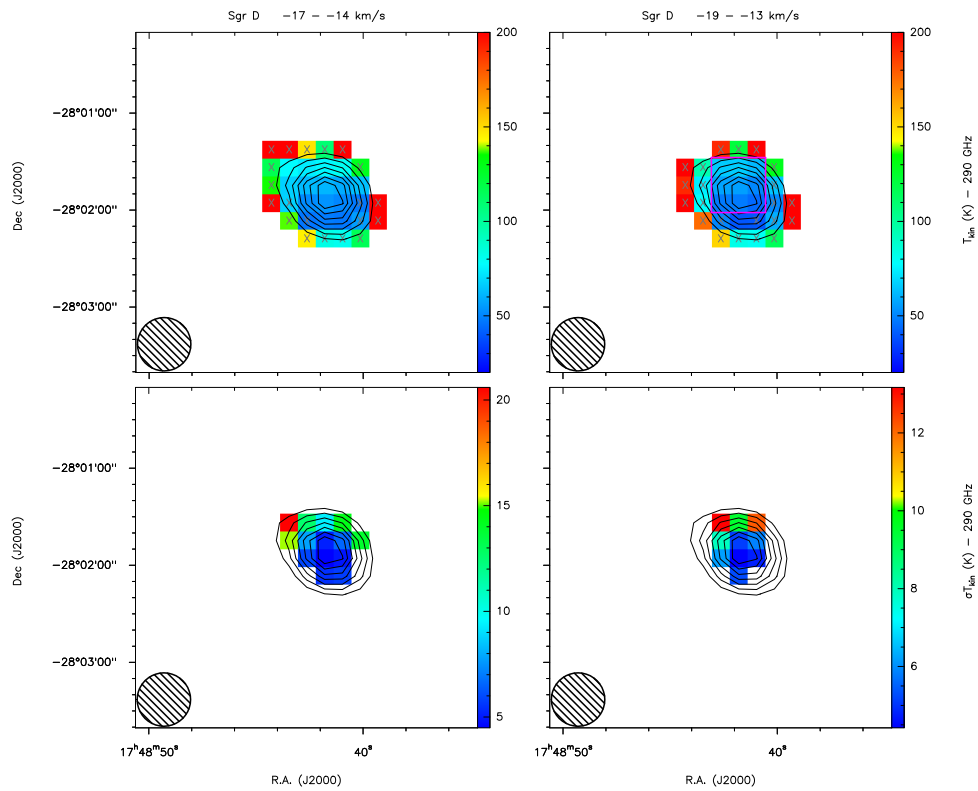


Fig. H.7. As Fig. H.1, for Sgr D.

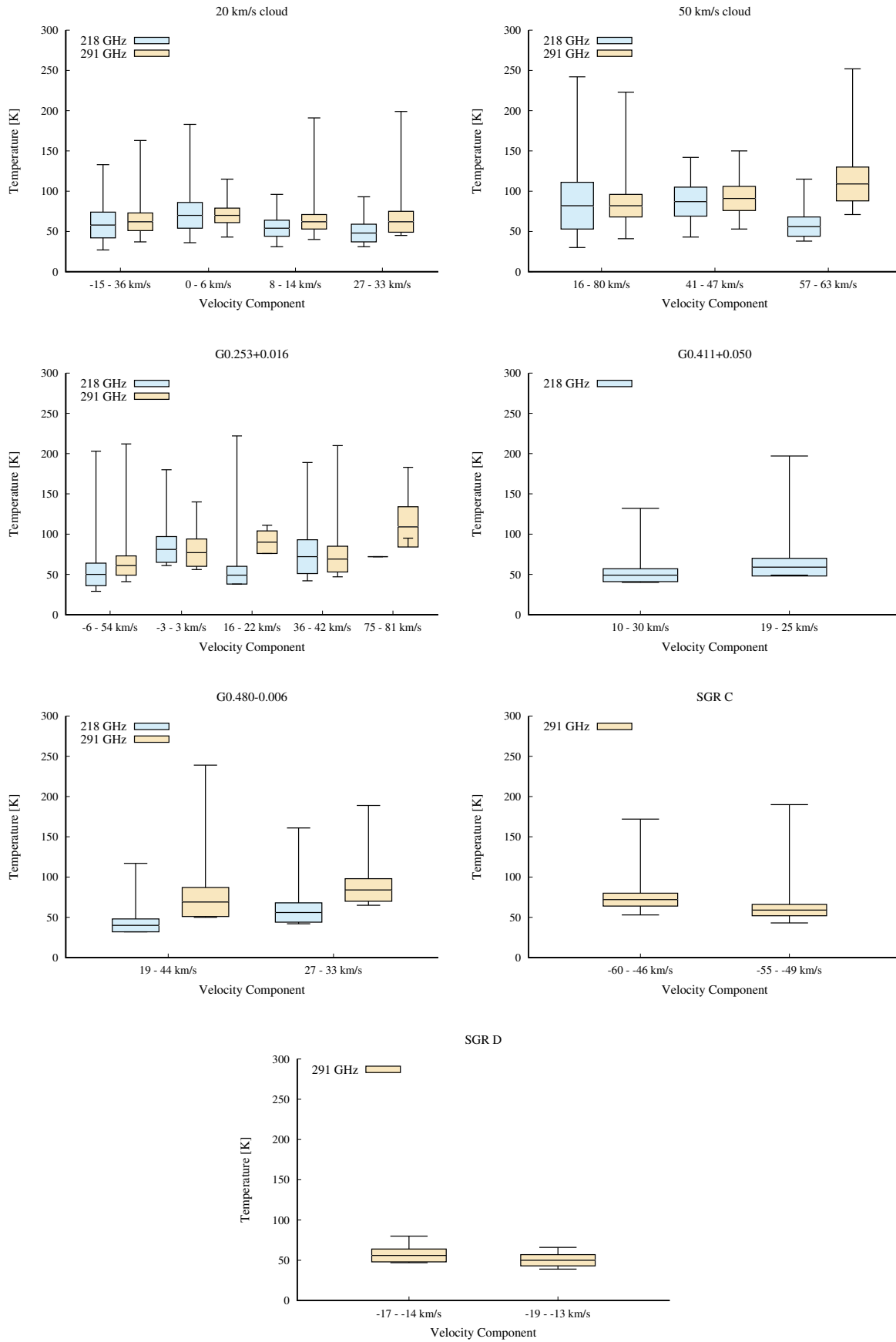


Fig. H.8. Minimal, weighted average, and maximal temperatures of the temperature maps of our seven sources. The vertical size of the boxes is given by the weighted average of the temperature $\pm 1\sigma$ uncertainty. The values are taken from Table 3. Blue and yellow boxes show the results at 218 and 291 GHz, respectively.

Appendix I: Temperature vs. line width**Table I.1.** Line ratios, temperatures, and line widths of Fig. 5 at 218 and 291 GHz.

Source	Velocity component (km s ⁻¹)	218 GHz			291 GHz		
		$R_{321, \text{Average}}$	T_{Average} (K)	Line width (km s ⁻¹)	$R_{422, \text{Average}}$	T_{Average} (K)	Line width (km s ⁻¹)
50 km s ⁻¹ cloud	41–47	0.409	104.9	24.6	0.464	113.4	20.9
		0.346	82.0	26.4	0.38	82.5	23.1
	57–63	0.279	61.7	10.1	0.440	103.2	20.5
		0.208	45.5	14.1	0.489	126.4	17.8
	-3–3	0.355	83.0	18.4			
G0.253+0.016	16–22	0.227	57.8	19.4			
		0.198	43.7	11.6			
	36–42	0.295	63.8	12.8	0.362	73.5	11.2
G0.411+0.050	19–25	0.458	67.4	11.7	0.264	53.5	10.6
		0.460	131.6	19.2	0.392	87.1	17.9
G0.480–0.006	27–33	0.255	55.6	7.3			
		0.333	74.9	11.6	0.416	92.9	12.3
Sgr C	-55--49	0.252	54.4	9.3	0.385	85.0	9.7
Sgr D	-19--13				0.299	62.9	8.2
					0.250	51.2	4.0